Department of Physics and Astronomy
University of Heidelberg

Master Thesis in Physics
submitted by

Stefan Dickopf

born in Bad Kreuznach (Germany)

2020

Design, installation and characterisation of a microwave transmission line for driving the transitions of the $^3\mathrm{He}^+$ hyperfine structure in a Penning trap

This Master thesis has been carried out by Stefan Dickopf at the
Max Planck Institute for Nuclear Physics in Heidelberg
under the supervision of
Prof. Dr. Klaus Blaum

Design, installation and characterisation of a microwave transmission line for driving the transitions of the $^3\mathrm{He}^+$ hyperfine structure in a Penning trap

A new Penning-trap experiment aiming at a measurement of the ground-state hyperfine structure of $^3\mathrm{He}^+$ and the nuclear magnetic moment of $^3\mathrm{He}^{2+}$ is being set up at the *Max Planck Institute for Nuclear Physics*. The hyperfine structure measurement will provide values for the bound state g-factors of the electron and nucleus with relative uncertainties of 10^{-10} and 10^{-9}, respectively. Additionally, the zero-field hyperfine splitting will be determined to 10^{-10} precision or better. As there has been no previous measurement on a system of interacting nuclear and electron spin in a Penning trap, calculations are made to connect the established theoretical results used in Penning trap g-factor experiments to the hyperfine structure measurement. In order to drive the hyperfine transitions, waveguides need to couple microwaves from a room temperature source to the cryogenic Penning traps over a distance of about 2 m. A numerical mode matching technique building on the mode propagation in waveguides is developed. Together with finite element calculations, it is used to optimise the waveguide for maximum transmission under the experimental constraints. It is argued that stainless steel oversized waveguide components are more practical than standard components and that the difficulties arising with them can be dealt with. Transmission measurements with the assembled system complement the numerical studies and show that the transmission line provides enough microwave power to drive the transitions of the hyperfine structure.

Design, Aufbau und Charakterisierungsmessungen der Mikrowelleneinkopplung zur Anregung der Übergänge der Hyperfeinstruktur von $^3\mathrm{He}^+$ in einer Penning-Falle

Ein neues Penning-Fallen Experiment zur Messung der Hyperfeinstruktur des Grundzustandes von $^3\mathrm{He}^+$ und des magnetischen Moments von $^3\mathrm{He}^{2+}$ wird derzeit am *Max-Planck-Institut für Kernphysik* aufgebaut. Aus der Hyperfeinstrukturmessung können die Werte der gebundenen Elektron und Kern g-Faktoren mit einer relativen Genauigkeit von 10^{-10} beziehungsweise 10^{-9} bestimmt werden. Außerdem wird die Hyperfeinstrukturaufspaltung des Grundzustands mit einer Genauigkeit von 10^{-10} oder besser bestimmt. Da bisher noch keine Messungen an einem System von interagierenden Kern und Elektron Spin in einer Penning-Falle existieren, werden Berechnungen angestellt um etablierte Resultate aus g-Faktor Penning-Fallen Experimenten für die Hyperfeinstrukturmessung zu nutzen. Um die Übergänge der Hyperfeinstruktur zu treiben, müssen Wellenleiter Mikrowellen über eine Distanz von etwa 2 m von der Quelle in die kryogenen Penning-Fallen koppeln. Eine numerische Mode Matching Technik, die auf der Propagation von Moden in Wellenleitern aufbaut, wird hergeleitet. Zusammen mit Rechnungen einer finite Elemente Methode wird diese genutzt um die Wellenleiter unter den experimentellen Restriktionen auf maximale Transmission zu optimieren. Es wird argumentiert, dass übergroße Edelstahl-Wellenleiter praktikabler als gebräuchliche Wellenleiter sind und die Schwierigkeiten die mit ihnen einhergehen gelöst werden können. Messungen der Transmission durch das aufgebaute System komplementieren die numerischen Studien und zeigen, dass die Mikrowellenleitung genug Leistung bereitstellt, um die Übergänge der Hyperfeinstruktur zu treiben.

Table of contents

List of Figures

1. Introduction

The implementation of the continuous Stern-Gerlach effect in a Penning trap enables the detection of the spin state of single isolated charged particles [1]. Using quantum-jump spectroscopy, the transition frequencies between the spin states are determined with high accuracy and the g-factors associated with the spin system can be extracted. Applying this technique has led to the most precise measurement of the g-factors of free [2] and bound [3] electrons, the positron [4] and, more recently, the g-factors of the proton [5, 6] and antiproton [7]. These measurements probe free and bound-state quantum electrodynamics at a very high precision [8] and, for the comparison of g-factors of particles and antiparticles, CPT violation [9].

At the *Max Planck Institute for Nuclear Physics* (MPIK) in Heidelberg a new Penning-trap experiment which uses the continuous Stern-Gerlach effect to perform quantum-jump spectroscopy on the charged states of ^{3}He is constructed. The singly charged state ^{3}He$^+$ constitutes a system of interacting nuclear and electron spin never investigated in a Penning trap before. By measuring the transition frequencies of the ground-state hyperfine splitting, the values for the bound g-factors of the electron and the nucleus are obtained with an aimed relative precision of 10^{-10} and 10^{-9}, respectively. Additionally, the zero field hyperfine splitting of the ground state will be determined to 10^{-10} precision or better. This will give an improvement in precision of at least a factor of 10 compared to the current most precise value obtained by spin-dependent collision processes of ^{3}He$^+$ with Cs atoms in a radio-frequency quadrupole trap [10]. While the measurement in the radio-frequency trap was operated in the weak field limit of the Zeeman effect, the strength of the magnetic field in this experiment requires a description in the intermediate regime. In the second phase of the experiment, the first direct measurement of the nuclear magnetic moment of ^{3}He^{2+} is planned with a relative precision of 10^{-9} or better. This will help to establish ^{3}He as a robust nuclear magnetic resonance (NMR) probe. Additionally, an altogether new direct comparison of the bound state g-factor of a nucleus to the free g-factor of the same nucleus is made possible, opening up tests of bound-state quantum electrodynamics with nuclear g-factors.

In the electronic ground state, the nucleus experiences the magnetic field produced by the spin magnetic moment of the orbiting electron. The energy associated with the nuclear magnetic moment in this field depends on the relative orientation of the electron and nuclear spin, resulting in the splitting of the ground-state energy. Using the ground state wavefunctions derived from the Schrödinger equation to evaluate the expectation value of the energy shift

yields the Fermi contact term E_F [11]. A more complete description of the energy splitting must include corrections from quantum electrodynamics δ_{QED}, recoil effects δ_{rec}, nuclear structure effects δ_{nucl} and from the strong interaction δ_{str}. In total, the ground-state hyperfine splitting is expanded as

$$\Delta E_{HFS} = E_F \left(1 + \delta_{nucl} + \delta_{QED} + \delta_{rec} + \delta_{str}\right). \tag{1.1}$$

The nuclear structure term is composed of the effects of nuclear polarisability, charge and magnetic moment distributions connected to charge and Zeemach radius, respectively, and contributes to ΔE_{HFS} at about 10^{-4} [12]. Thus this measurement will be highly sensitive to investigate these effects.

Nuclear magnetic resonance probes allow for high-precision absolute magnetic field measurements. These measurements rely on the value of the shielded nuclear magnetic moment of the probe. The shielding of the magnetic field is in first approximation provided by the electron cloud surrounding the nucleus, resulting in the so-called diamagnetic shielding described by the parameter σ. For the currently most common probes based on water, the diamagnetic shielding σ of the proton nuclear magnetic moment needs to be extracted from measurements that are highly sensitive to temperature, probe shape, pressure and other effects [13]. In contrast, ^{3}He is a much simpler atomic system for which σ can be theoretically calculated to high precision and its dependence on the aforementioned systematic effects is lower by a factor of about 10 [14, 15]. Currently, the value of the nuclear magnetic moment of ^{3}He has only been measured by a comparison of the NMR frequencies with water or molecular hydrogen samples [16]. A direct measurement performed at this experiment will enable the use of ^{3}He as an uncorrelated NMR probe. The next-generation experiments located at Fermilab [17] and J-Parc [18] aim at the measurement of the muon anomalous magnetic moment with a relative precision of 10^{-7}. Here, the difference of the Larmor precession frequency and the cyclotron frequency of muons in a magnetic field, which is a value proportional to the magnetic field, is measured. ^{3}He probes offer the possibility to measure the magnetic field with high-precision as an uncorrelated alternative to the already well developed water NMR probes.

Structure of this thesis

In this work, the theoretical and experimental requirements for driving the transitions of the hyperfine structure are worked out. Chapter 2 introduces the basic physics of Penning traps required for the cyclotron frequency measurement. In Chapter 3, the hyperfine structure of ^{3}He$^+$ is investigated. Starting from the general level structure of ^{3}He$^+$ in a magnetic field, the expected lineshapes of the spin-flip resonances inside a Penning trap are worked out and the measurement scheme is described. To drive the transitions, microwaves need to be coupled into the trap with waveguides. Chapter 4 deals with the theoretical description of waveguides and provides a numerical tool for calculating transmission through arbitrarily shaped circular waveguides. As the requirements for the microwave power inside the Penning trap are quite strict, an optimisation of the waveguide is necessary and carried out in Chapter 5. By applying the techniques of Chapter 4 and finite element method calculations, the waveguide is optimised for maximum transmission. The results of the optimisation are checked with explicit measurements in Chapter 6.

2. The Penning trap

A Penning trap stores ions by superimposing a static axial magnetic field with a static quadrupolar electric potential. Applied microwave excitations drive the hyperfine transitions of the stored $^3\text{He}^+$ ion. The spin-flip detection and determination of the magnetic field strength necessary for calculating the magnetic moments rely on the measurement of the eigenfrequencies of the ion inside the trap. This chapter introduces the basic physics necessary to perform such measurements.

2.1. Ion motion inside a Penning trap

A charged particle moving in a magnetic field $\boldsymbol{B} = B\boldsymbol{e}_z$ along the axial direction is forced on a circular motion in the xy-plane with the angular velocity

$$\omega_c = \frac{q}{m}B. \tag{2.1}$$

Here q is the charge and m the mass of the ion. The frequency ω_c is termed free cyclotron frequency.

To trap the particle in the axial direction as well an electric potential is used. However, Maxwell's equations do not allow for electric fields that solely provide a restoring force in a singular direction. The addition of a quadrupolar electric potential

$$\Phi(z, \rho) = V_0 C_2 \left(z^2 - \rho^2/2 \right), \tag{2.2}$$

with a free geometric parameter C_2 and voltage V_0, leads to a restoring force in the axial direction and an outward radial force opposite to the force provided by the magnetic field. This results in an oscillation in the axial direction with frequency

$$\omega_z = \sqrt{2\frac{q}{m}C_2 V_0}. \tag{2.3}$$

Additionally, the radial motion in the xy-plane is split into a sum of two circular motions described by the so-called reduced cyclotron ω_+ and magnetron ω_- frequency, respectively,

$$\omega_\pm = \frac{1}{2}\left(\omega_c \pm \sqrt{\omega_c^2 - 2\omega_z^2} \right). \tag{2.4}$$
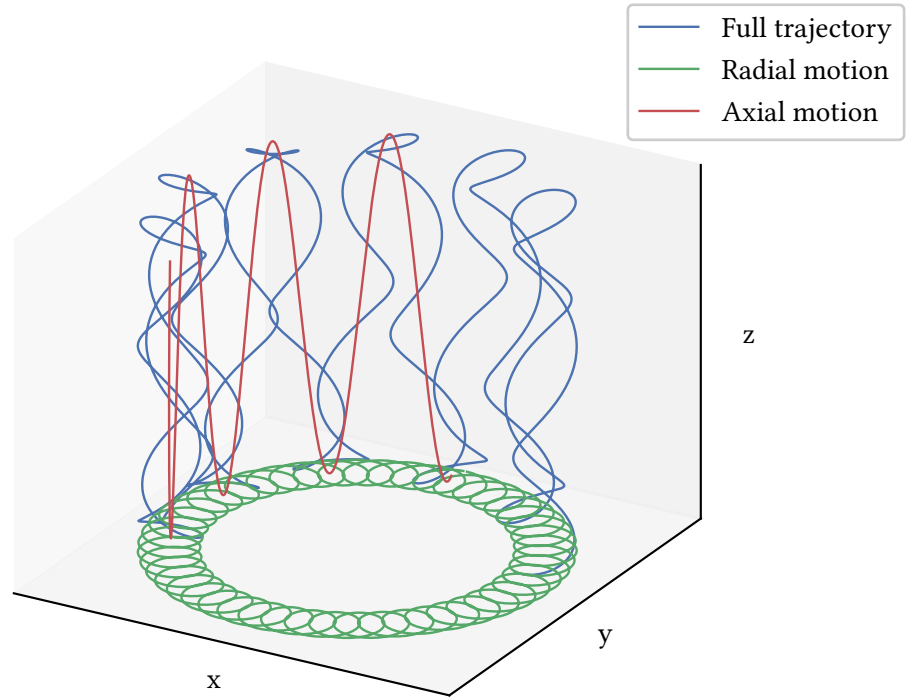
Figure 2.1: Motion of an ion inside a Penning trap. The blue curve shows the full trajectory. In the xy-plane, the green curve shows the radial motion consisting of the fast reduced cyclotron and the slow magnetron motion. The axial motion is plotted in red. In order to produce a better visualisation of the motion, the cyclotron frequency used for this graphic was reduced by about a factor of 10 compared to the actual value in this experiment.

The ion is trapped only if the magnetic field is large enough compared to the electrostatic potential such that $\omega_c^2 > 2\omega_z^2$. Typically, the frequencies obey $\omega_+ \gg \omega_z \gg \omega_-$. Figure 2.1 shows the ion's trajectory produced by the superposition of the three eigenmotions.

The free cyclotron frequency can be determined by a measurement of the eigenfrequencies and relating them according to

$$\omega_c = \omega_+ + \omega_-, \quad \omega_c^2 = \omega_+^2 + \omega_-^2 + \omega_z^2. \tag{2.5}$$

The latter is an invariance theorem as it is also valid for slight errors of the trap configuration [19]. Using Eq. (2.1) and the charge to mass ratio $\frac{q}{m}$ yields the value of the magnetic field at the ion's position.
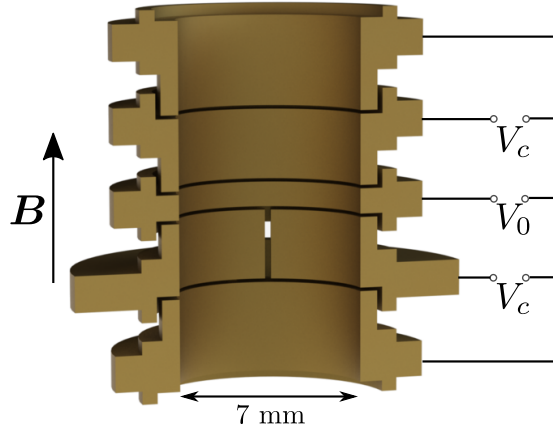
Figure 2.2: Cut of a cylindrical Penning trap with five electrodes. The centre ring electrode is kept at a potential V_0 relative to the upper and lower electrodes, called endcaps. The two electrodes between ring and endcap are termed correction electrodes and are at a potential V_c relative to the endcaps. The lower correction electrode is split such that a specific RF excitation field can be generated.

2.2. Cylindrical Penning trap

The homogeneous magnetic field is generated by a superconducting magnet system. To generate the electrostatic potential given in Eq. (2.2) a stack of cylindrical trap electrodes is used, see Figure 2.2. A ring electrode at potential V_0 relative to the upper and lower endcap electrodes allows for tuning of the axial frequency of the ion. Two correction electrodes at the potential V_c relative to the endcaps are used to set the tuning ratio TR $= V_c/V_0$. Together they produce a symmetric potential that is expanded as

$$\Phi(z) = V_0 \sum_n C_{2n} z^{2n} = V_0 \left(C_2 z^2 + C_4 z^4 + C_6 z^6 + ... \right) \tag{2.6}$$

on axis [20]. Here $z = 0$ is the center of the ring electrode and defines the ion's position of rest.

With optimised trap electrode lengths a tuning ratio can be found such that the axial frequency of the ion determined by the parameter C_2, compare Eq. (2.3), is independent of the correction voltage V_c, while at the same time the first higher order terms C_4 and C_6 are cancelled [21]. A Penning trap that meets these conditions is said to be orthogonal and optimised. Any residual C_4, C_6 or higher order terms lead to anharmonicities of the axial oscillation that result in amplitude dependant shifts of the axial frequency [22].

2.3. Eigenfrequency detection

As the ion moves inside the trap, its charge q induces tiny image currents in the trap electrodes [5]. The detection of these currents is possible by measuring the voltage drop over a large resistance. For the purpose of measuring the axial frequency, a coil is connected to one of

the endcap or correction electrodes, forming a parallel RLC circuit with the trap capacitance. By tuning the ion's frequency to the resonance frequency of the RLC circuit, the image current

$$I_{\text{ind}} = \frac{q}{D}\dot{z},\tag{2.7}$$

where D is the effective electrode distance [20], produces a voltage drop

$$U_{\text{ind}} = R_{\text{p}}I_{\text{ind}}\tag{2.8}$$

over the parallel resistance R_{p} of the tuned circuit. Here $\dot{z}$ is the time derivative of the ion's axial position z. The additional voltage on the endcap electrode results in a force

$$F = \frac{q}{D}U_{\text{ind}}\tag{2.9}$$

on the electrons motion. Using Eq. (2.7) the harmonic oscillation of the ion's axial coordinate z is replaced by a damped oscillation described by

$$\ddot{z} + \frac{R_{\text{p}}q^2}{mD^2}\dot{z} + \omega_z^2 z = 0.\tag{2.10}$$

This defines the damping constant

$$\gamma = \frac{R_{\text{p}}q^2}{mD^2},\tag{2.11}$$

which is a measure for the interaction of the ion with the resonator.

The thermal Johnson noise on the detection system drives the damped oscillation. By letting the ion's axial motion come into thermal equilibrium with the detection system, it effectively provides a short circuit for the thermal noise on the resonator. In the Fourier spectrum of the measured thermal voltages, a so-called *dip* appears at the ion's axial frequency [23]. Using sideband coupling to the magnetron and cyclotron motion with RF excitations results in a modulation of the axial frequency. The two frequency components appear as separate dips (*double dip*) in the frequency spectrum and give access to either the magnetron or the cyclotron frequency [24].

Phase-sensitive measurements use coupling pulses to transfer the cyclotron motion's phase acquired after a free evolution period to the axial motion. The coupling pulse excites the axial motion of the ion such that it dominates the thermal noise of the resonator enabling much faster integration times of the Fourier spectrum. Systematic errors arising with the *pulse and phase* method [25] can be avoided with the newer *pulse and amplify* method [26].

3. Hyperfine structure of $^3\mathrm{He}^+$ inside a Penning trap

Brown and Gabrielse [27, 28] calculated the spin-flip lineshape of a single charged spin-$\frac{1}{2}$ particle inside a Penning-trap. Fitting this lineshape to the measured spin-flip spectrum gives access to the frequency of the transition. In order to use this calculation for the hyperfine splitting of $^3\mathrm{He}^+$, which is described by the interaction of its spin-$\frac{1}{2}$ nucleus with the spin-$\frac{1}{2}$ electron, the possible transitions have to be modelled as separate spin-$\frac{1}{2}$ systems.

Starting from the Hamiltonian of the interacting electron-nucleus system, the effective two-level Hamiltonians of the hyperfine transitions are derived and then used to calculate the lineshape. Lastly, the scheme to measure the transition resonance is described.

3.1. Static magnetic field

In a simple hydrogen-like atom or ion with non-vanishing nuclear spin, a splitting of the level structure arises due to the magnetic moment of the nucleus interacting with the magnetic field generated by the orbiting electron. Even for zero orbital angular momentum of the electron, it generates a magnetic field, attributed to its spin, at the position of the nucleus. In this case the Hamiltonian

$$\hat{H} = A \left(\hat{\boldsymbol{\sigma}}^e \cdot \hat{\boldsymbol{\sigma}}^I \right) - \left(\mu_e \hat{\boldsymbol{\sigma}}^e + \mu_I \hat{\boldsymbol{\sigma}}^I \right) \cdot \boldsymbol{B} \tag{3.1}$$

describes the hyperfine splitting of an electron bound to a spin-$\frac{1}{2}$ nucleus in an external magnetic field $\boldsymbol{B}$ [29]. Here $\hat{\boldsymbol{\sigma}}^e$ and $\hat{\boldsymbol{\sigma}}^I$ are the Pauli matrices associated with the electron and nuclear spin, respectively, and μ_e, μ_I the magnetic moments of the spins. The first term describes the interaction of the electron and the nuclear spin with a coupling constant A to be later connected with the zero-field hyperfine splitting and the second term the interaction of the electron and the nuclear spin with the external magnetic field. The Hamiltonian is an operator on the product states of the electron and the nuclear spin which will be written as $|s_z\rangle_e \otimes |s_z\rangle_n = |s_{z,e} s_{z,n}\rangle$, where $|s_z\rangle$ will be either $|+\rangle$ or $|-\rangle$ corresponding to spin up or spin down.

In the following, the magnetic field will be assumed to be static. Then its direction can be chosen to coincide with the z-axis, i.e. $\boldsymbol{B} = B\boldsymbol{e}_z$. In the basis $\{|++\rangle, |+-\rangle, |-+\rangle, |--\rangle\}$ and with

the definitions $\mu = -\mu_e - \mu_I$, $\mu' = -\mu_e + \mu_I$, the matrix representation of the Hamiltonian

$$\hat{H} \triangleq \begin{pmatrix} A + B\mu & 0 & 0 & 0 \\ 0 & -A + B\mu' & 2A & 0 \\ 0 & 2A & -A - B\mu' & 0 \\ 0 & 0 & 0 & A - B\mu \end{pmatrix} \tag{3.2}$$

shows that two of its eigenstates will generally be mixtures of the $|+-\rangle$ and $|-+\rangle$ states. The diagonalisation of the Hamiltonian reduces to the diagonalisation of the centre 2×2 matrix. Using the definitions

$$\sinh\theta = \frac{B\mu'}{2A}, \quad r_{\pm} = \frac{1}{\sqrt{2}}\sqrt{1 \pm \tanh\theta} \tag{3.3}$$

and some algebra the eigenstates and the corresponding energies are calculated and listed in Table 3.1.

State	Energy
$|1\rangle = |++\rangle$	$A(+1 + 2\frac{\mu}{\mu'}\sinh\theta)$
$|2\rangle = r_+ |-+\rangle - r_- |+-\rangle$	$A(-1 - 2\cosh\theta)$
$|3\rangle = r_+ |+-\rangle + r_- |-+\rangle$	$A(-1 + 2\cosh\theta)$
$|4\rangle = |--\rangle$	$A(+1 - 2\frac{\mu}{\mu'}\sinh\theta)$

Table 3.1: Eigenstates for the Hamiltonian given in Eq. (3.2).

It is now worthwhile to consider the case of $^3\text{He}^+$ specifically. At zero magnetic field, the states $|1\rangle$, $|3\rangle$ and $|4\rangle$ are degenerate and the difference of their energy to the state $|2\rangle$ corresponds to the zero-field hyperfine splitting ΔE_{HFS}. In contrast to hydrogen, the constant A is negative for $^3\text{He}^+$ and it connects to ΔE_{HFS} as $A = -\frac{1}{4}\Delta E_{\text{HFS}}$. The sign of $\sinh\theta$ is therefore negative and r_+ approaches zero for large magnetic fields, whereas r_- approaches unity. The Breit-Rabi diagram of the level scheme is shown in Figure 3.1.

3.2. Coupling to a microwave field

To drive a transition between the different states of the hyperfine splitting an oscillating magnetic field perpendicular to the static field is needed. Using a classical description of the microwave field, the Hamiltonian still has the form given in Eq. (3.1). Without loss of generality, the field oscillating with frequency ω and strength B_{RF} can be chosen to lie in the x-plane. Thus, an interaction term

$$\hat{H}_{I,\text{RF}} = -B_{\text{RF}}\cos(\omega t)\left(\mu_e\hat{\sigma}_x^e + \mu_I\hat{\sigma}_x^I\right) \tag{3.4}$$

is added to the static magnetic field Hamiltonian described by Eq. (3.2). The matrix representation of $\hat{H}_{I,\text{RF}}$ in the basis spanned by the eigenvectors of the time independent Hamiltonian Eq. (3.2), compare Table 3.1, is

$$\hat{H}_{I,\text{RF}} \triangleq -B_{\text{RF}}\cos(\omega t)\begin{pmatrix} \hat{\sigma}_x(\mu_e r_+ - \mu_I r_-) & \hat{\sigma}_z\mu_e r_- + \mathbb{1}\mu_I r_+ \\ \hat{\sigma}_z\mu_e r_- + \mathbb{1}\mu_I r_+ & \hat{\sigma}_x(\mu_e r_+ + \mu_I r_-) \end{pmatrix}, \tag{3.5}$$
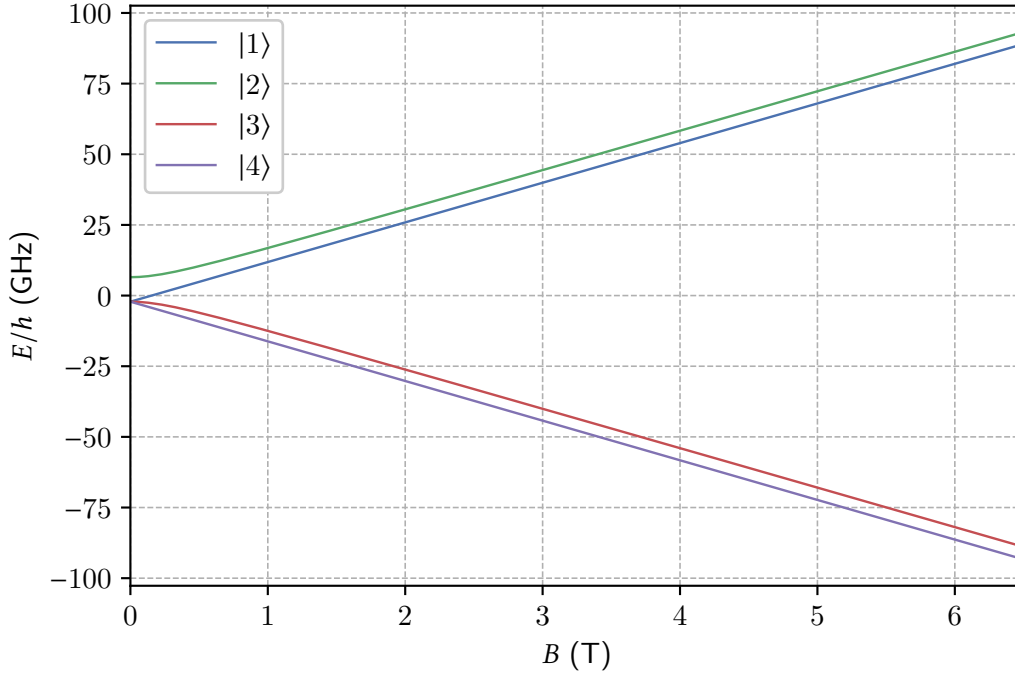
Figure 3.1: Breit-Rabi diagram of $^3\text{He}^+$. At zero field the energies of the three lower states are degenerate. The energy difference between the two negative/positive states is nearly constant for high fields. In contrast, the energy difference from one negative to one positive energy state grows linearly with magnetic field.

where $\hat{\sigma}_x$, $\hat{\sigma}_z$ and $\mathbb{1}$ are 2×2 matrices.

The transition probabilities are best calculated in the interaction (Dirac) picture, where they are given by the matrix element of the time evolution operator that solves

$$i\hbar \frac{d}{dt}\hat{U}_I(t) = \hat{H}_{ID}(t)\hat{U}_I(t). \tag{3.6}$$

Here, $\hat{H}_{ID} = \hat{U}_0(t)^\dagger \hat{H}_{I,\text{RF}} \hat{U}_0(t)$ is the interaction Hamiltonian in the Dirac picture, with $\hat{U}_0(t)$ being the time evolution operator of the time-independent system. In the chosen basis, $\hat{U}_0(t)$ is diagonal and has entries $(\hat{U}_0(t))_{ii} = \exp(-iE_i t/\hbar)$. This yields

$$\hat{H}_{ID,\text{RF}} \hat{=} - B_{\text{RF}}\cos(\omega t)\begin{pmatrix} 0 & -U_{12}M_-^n & U_{13}M_+^e & 0 \\ -U_{21}M_-^n & 0 & 0 & -U_{24}M_-^e \\ U_{31}M_+^e & 0 & 0 & U_{34}M_+^n \\ 0 & -U_{42}M_-^e & U_{43}M_+^n & 0 \end{pmatrix}, \tag{3.7}$$

with $U_{ij} = \exp\left(i(E_i - E_j)t/\hbar\right)$. The coefficients $M_\pm^{e/n}$ are defined as $M_\pm^e = \mu_e r_- \pm \mu_I r_+$ for the high frequency (electron spin-flips) transitions and $M_\pm^n = \mu_I r_- \pm \mu_e r_+$ for the low frequency (nuclear) transitions.

Generally it is very hard (or just not possible) to analytically solve Eq. (3.6) for systems with more than two states. Usually, larger systems can be approximated as two-state systems if the frequency of the oscillating field is close to resonance with one of the transitions. This is done with a rotating wave approximation (RWA) [30]. To see that a RWA can be applied, the cosine in Eq. (3.7) is written as $\cos(\omega t) = \frac{1}{2}\left(e^{i\omega t} + e^{-i\omega t}\right)$ and ω is set equal to one of the transition frequencies. The Hamiltonian can then be written in terms of a time independent part and fast oscillating parts. For example, the transition from the state $|1\rangle$ to $|2\rangle$ with frequency $\omega = (E_2 - E_1)/\hbar$ is approximated by

$$\hat{H}_{ID,\mathrm{RF}} = \frac{1}{2}B_{\mathrm{RF}}M_-^n\left(|1\rangle\langle 2| + |2\rangle\langle 1|\right) + \text{fast oscillating terms.} \tag{3.8}$$

The RWA is valid if the Rabi frequency defined by $\Omega_{12} = B_{\mathrm{RF}}M_-^n/\hbar$ (or similarly for the other transitions) is much smaller than the frequency of the transition ω. This can be safely assumed to be the case for this experiment, as shown later in Table 3.2. Applying the RWA by dropping all the fast oscillating terms reduces the four-level system to a two-level system.

3.3. Effect of oscillations in the magnetic bottle

To be able to detect the state of the spin, a quadratic magnetic field in the z-direction, termed the magnetic bottle, is needed inside one of the traps. Thus the ion experiences a time dependant magnetic field

$$B(t) = B_0 + B_2 z(t)^2. \tag{3.9}$$

Adding the additional z-field component to the Hamiltonian given in Eq. (3.2) in its eigenbasis results in an additional interaction term for the Dirac picture Hamiltonian, compare Eq. (3.7)

$$\hat{H}_{ID,2} \,\hat{=}\, -B_2 z(t)^2 \begin{pmatrix} -\mu & 0 & 0 & 0 \\ 0 & \tanh\theta\mu' & 2r_+r_-U_{23}\mu' & 0 \\ 0 & 2r_+r_-U_{32}\mu' & -\tanh\theta\mu' & 0 \\ 0 & 0 & 0 & \mu \end{pmatrix}. \tag{3.10}$$

The axial frequency is about 4 orders of magnitude smaller than the frequencies of the hyperfine transitions. It is thus not possible to omit the terms on the diagonal with a RWA. The terms off-axis have additional oscillating contributions at the large frequency ω_{23} and could be omitted. Now, a redefinition of the non-interacting Hamiltonian and the interaction Hamiltonian in the Schrödinger picture according to

$$\hat{H}_0 \,\hat{=}\, \begin{pmatrix} E_1 & 0 & 0 & 0 \\ 0 & E_2 & 0 & 0 \\ 0 & 0 & E_3 & 0 \\ 0 & 0 & 0 & E_4 \end{pmatrix} - B_2 z(t)^2 \begin{pmatrix} -\mu & 0 & 0 & 0 \\ 0 & \tanh\theta\mu' & 0 & 0 \\ 0 & 0 & -\tanh\theta\mu' & 0 \\ 0 & 0 & 0 & \mu \end{pmatrix}, \tag{3.11}$$

$$\hat{H}_I \,\hat{=}\, -B_{\mathrm{RF}}\cos(\omega t)\begin{pmatrix} 0 & -M_-^n & M_+^e & 0 \\ -M_-^n & 0 & 0 & -M_-^e \\ M_+^e & 0 & 0 & M_+^n \\ 0 & -M_-^e & M_+^n & 0 \end{pmatrix} - B_2 z(t)^2 \begin{pmatrix} 0 & 0 & 0 & 0 \\ 0 & 0 & 2r_+r_-\mu' & 0 \\ 0 & 2r_+r_-\mu' & 0 & 0 \\ 0 & 0 & 0 & 0 \end{pmatrix}, \tag{3.12}$$

changes only the definition of the time-evolution operator $\hat{U}_0$ and the elements U_{ij}, as the eigenstates themselves are not changed:

$$(\hat{U}_0(t))_{ii} = \exp\left(\frac{i}{\hbar}\int_0^t d\bar{t}(E_i + \delta E_i(\bar{t}))\right) = \exp\left(iE_i t/\hbar\right)\exp\left(\frac{i}{\hbar}\int_0^t d\bar{t}\delta E_i(\bar{t})\right), \qquad (3.13)$$

$$U_{ij}(t) = \exp\left(i\omega_{ij}t\right)\exp\left(i\int_0^t d\bar{t}\delta\omega_{ij}(\bar{t})\right), \qquad (3.14)$$

with $\omega_{ij} = (E_i - E_j)/\hbar$ and $\delta E_i(t)$, $\delta\omega_{ij}(t)$ defined from the time dependant part of $\hat{H}_0$.

Back in the Dirac picture the factors U_{ij} need to be added to the interaction Hamiltonian as in Eq. (3.7) and Eq. (3.10). The RWA is still applicable because U_{ij} still includes the same fast oscillating term at the transition frequency which leads to slow oscillating terms when multiplied with the cosine from the microwave field. The factor that includes the integral in U_{ij} can be assumed to oscillate maximally at the axial frequency of the particle, which is always much slower than the hyperfine transitions frequencies. Therefore, the second term in the interaction Hamiltonian Eq. (3.12) still completely drops out as argued before. It is thus still possible to approximate the four-level system as separate two-level systems, if the frequency of the applied microwave field is close to one of the transition frequencies.

The effective two-level interaction Hamiltonian in the Dirac picture for the transition $i \rightarrow j$ with $\omega_{ij} = (E_i - E_j)/\hbar$ can be written as

$$\hat{H}_{ID,RWA} \,\hat{=}\, \frac{\hbar\Omega_{ij}}{2}\begin{pmatrix} 0 & e^{i\Delta_{ij}t + i\int_0^t d\bar{t}\delta\omega_{ij}(\bar{t})} \\ e^{-i\Delta_{ij}t - i\int_0^t d\bar{t}\delta\omega_{ij}(\bar{t})} & 0 \end{pmatrix}, \qquad (3.15)$$

where Ω_{ij} is the Rabi frequency of the transition as explained in the previous section and $\Delta_{ij} = \omega - \omega_{ij}$ defines the detuning. Each of the transitions is now effectively modelled by a Hamiltonian which is equivalent to the that of a single spin-$\frac{1}{2}$ particle in a Penning trap under the influence of an external microwave excitation.

3.4. Spin-flip lineshape

Having obtained effective two-level Hamiltonians for the hyperfine transitions, the calculation of the lineshape now follows that of Brown and Gabrielse [27, 28]. In the following, the term *spin-flip* is meant as a transition from one of the four hyperfine states to another. Technically, these are not spin-flips in the sense that a single spin changes its orientation in the magnetic field, as the states $|2\rangle$ and $|3\rangle$ are still very much superposition states at the relevant magnetic field of ≈ 5 T. For example, at 5 T the state $|2\rangle \approx 0.03084\,|-+\rangle - 0.99952\,|+-\rangle$ is mostly equal to the $|+-\rangle$ state. The main contribution, in the sense of the matrix element in Eq. (3.7), to the transition to the $|++\rangle$ state however is the $|-+\rangle$ flip to $|++\rangle$, because $|\mu_e/\mu_I| \approx 864$.

The lineshape arises due to the varying transition frequency over the course of one spin-flip excitation. This change in frequency, as mentioned before, is caused by the oscillation of the ion inside the magnetic bottle. While this oscillation would cause the frequency to oscillate in time, an excitation could still be coherent. This coherency is lost due to the coupling of the axial motion to the detection system, which constitutes a heat bath and causes the amplitude

of the axial motion to randomly change. The averaged maximum of $\delta\omega(t)$ is a measure for the spread of the transition frequency due to the oscillation in the magnetic bottle and thus called the linewidth parameter $\Delta\omega$, which is proportional to the average of the thermally distributed axial amplitude

$$\langle z^2 \rangle = \frac{kT}{m\omega_z^2}.$$

(3.16)

The time constant defined by the inverse of the coupling to the resonator $1/\gamma$, compare Eq. (2.11), is connected to a dephasing time. Random jumps of the transition frequency due to the thermal noise on the resonator, occurring with frequency γ, lead to acquisition of random phase between the two spin states and thus decreasing expectation value of transverse spin. The natural linewidth of the transitions can be neglected, as the lifetimes of the states are very large in comparison to $1/\Delta\omega$ and $1/\gamma$. As derived by Brown [28], defining the line profile as the Fourier transformation

$$\chi(\Delta_{\text{RF}}) = \frac{1}{2\pi} \int_{-\infty}^{\infty} dt e^{i\Delta_{\text{RF}}t} \, \tilde{\chi}(t)$$

(3.17)

of the correlation function[1]

$$\tilde{\chi}(t) = \left\langle \exp\left\{ i \int_0^t d\bar{t}\, \delta\omega(\bar{t}) \right\} \right\rangle$$

(3.18)

provides the spin-flip probability at a detuning Δ_{RF} after excitation of τ seconds

$$P(\Delta_{\text{RF}}, \tau) = \frac{1}{2} \left\{ 1 - \exp\left[-\pi\Omega^2 \chi(\Delta_{\text{RF}})\tau \right] \right\}.$$

(3.19)

The brackets in the correlation function denote a classical statistical averaging over the random variable $z(t)$ appearing inside $\delta\omega(t)$. In this way, Eq. (3.18) includes correlations of the random amplitudes of the axial motion.

In the analysis and precision trap, different line profiles arise. The strong magnetic bottle B_2 required for measuring spin-flips inside the analysis trap results in the linewidth parameter being much larger than the coupling constant, i.e. $\gamma \ll \Delta\omega$. Over a single oscillation cycle of the complex exponential in Eq. (3.18) with frequency $\sim \Delta\omega$, the amplitude of $\delta\omega(t)$ is therefore constant and $\delta\omega(t)$ can be replaced by a time averaged value. This leaves an averaging over many oscillation periods, where for every period the axial amplitude takes a new random value drawn from the thermal (Boltzmann) distribution of axial energies. This averaging may now be switched with the time integration appearing in Eq. (3.17) leading to

$$\chi(\Delta_{\text{RF}}) = \frac{\theta(\Delta_{\text{RF}})}{\Delta\omega} \exp\left(-\frac{\Delta_{\text{RF}}}{\Delta\omega} \right),$$

(3.20)

where Δ is the detuning and θ the step function.

In the precision trap there is only a residual B_2. For the low frequency nuclear spin transitions this leads to $\gamma \gg \Delta\omega$. Over one oscillation of the complex exponential in Eq. (3.18) the

---

[1]The integrand of Eq. (3.17) is just the matrix element of the Hamiltonian Eq. (3.15).

frequency $\delta\omega(t)$ fluctuates fast, and thus averages quickly to $\Delta\omega$. The line profile function of the correlation function $\exp(-i\Delta\omega t)$ is thus just the shifted delta function

$$\chi(\Delta_{\mathrm{RF}}) = \delta(\Delta_{\mathrm{RF}} - \Delta\omega). \tag{3.21}$$

For large times the correlation function is expected to vanish, as the uncorrelated thermal noise driving the axial motion will eventually dominate the correlated oscillations of $z(t)$. Therefore a next order correction to the correlation function is the addition of the factor $\exp\left(-\frac{\Delta\omega^2}{\gamma}|t|\right)$. This leads to a Lorentzian line profile

$$\chi(\Delta_{\mathrm{RF}}) = \frac{1}{\pi} \frac{\Delta\omega^2/\gamma}{(\Delta_{\mathrm{RF}} - \Delta\omega)^2 + (\Delta\omega^2/\gamma)^2}. \tag{3.22}$$

However, for the electron spin transitions the linewidth parameter $\Delta\omega > \gamma$, but much less than in the analysis trap. Then the line profile can not be computed for a limiting case, but the result for arbitrary $\Delta\omega$ and γ needs to be used. Brown and Gabrielse's general result is

$$\chi(\Delta_{\mathrm{RF}}) = \frac{4}{\pi} \operatorname{Re} \frac{\gamma'\gamma}{(\gamma' + \gamma)^2} \sum_{n=0}^{\infty} \frac{(\gamma' - \gamma)^{2n}(\gamma' + \gamma)^{-2n}}{(n + 0.5)\gamma' - 0.5\gamma - i\Delta_{\mathrm{RF}}}, \tag{3.23}$$

where $\gamma' = \sqrt{\gamma^2 + i4\gamma\Delta\omega}$.

In order to understand the consequences of the different line profiles and their implications on the experimental realisation, the relevant parameters for the analysis and precision trap are calculated. The lineshape parameter $\Delta\omega$ can be read off from the time dependant part of $\hat{H}_0$ in Eq. (3.11), where $z(t)^2$ is substituted by its average Eq. (3.16). Similarly, the Rabi frequencies are the elements of the first term in the interaction Hamiltonian Eq. (3.12).

Table 3.2 lists the parameters for this experiment. The nuclear transitions have a very small linewidth compared to the electron spin transitions. This can be understood in the following way.z The electron only sees the external magnetic field B. In contrast, the nucleus also experiences the field generated by the orbiting electron, which dominates the external field. Thus, changes in the external field induce only slight changes of the transition frequency, see also Figure 3.1. As the coupling constant is expected to be $\gamma \approx 5$, the above cases for the line profiles are justified. The very large linewidths of the electron spin transitions inside the analysis trap motivate the requirement of a precision trap with very small B_2. Figure 3.2 shows the theoretical spin-flip line profiles for the analysis and precision trap. Clearly, the lineshape of the nuclear transitions inside the precision trap have a very reduced width, which is due to the additional factor $\Delta\omega/\gamma$ appearing in Eq. (3.22), while the width of the electronic transitions in the PT is nearly equal to $\Delta\omega$.

In the analysis trap, the spin-flip probability given in Eq. (3.19) should be as large as possible such that spin-flips can be driven efficiently on a large range of frequencies, whereas in the precision trap it should not be oversaturated away from resonance to achieve the best frequency resolution. However, the tiny linewidth of the nuclear transitions in the precision trap might require an oversaturation as well. Quantifying this with the requirement that the argument of the exponential in Eq. (3.19) should be approximately (or bigger than) negative unity on

Transition	ν_{AT} (GHz)	$\Delta\nu_{\text{AT}}$ (kHz)	ν_{PT} (GHz)	$\Delta\nu_{\text{PT}}$ (Hz)	Ω/B_{RF} (rad/s/nT)
$4 \rightarrow 3$	4.387	18.90	4.401	$16.56 \cdot 10^{-3}$	2.48
$1 \rightarrow 2$	4.278	18.90	4.264	$16.56 \cdot 10^{-3}$	2.28
$3 \rightarrow 1$	148.8	$9.65 \cdot 10^3$	156.1	8.77	88.0
$4 \rightarrow 2$	157.5	$9.65 \cdot 10^3$	164.8	8.77	88.0

Table 3.2: Transition frequencies ν, lineshape parameter $\Delta\nu$ and Rabi frequency per microwave field Ω for the four different transitions in the analysis (AT) and precision (PT) trap. The following parameters were used: External magnetic field $B_{\text{AT}} = 5.46$ T, $B_{\text{PT}} = 5.72$ T, magnetic bottle $B_{2,\text{AT}} = 110$ kT/m^2, $B_{2,\text{PT}} = 0.1$ T/m^2, temperature $T = 10$ K, axial frequency $\nu_z = 472$ kHz. These are expected values for this experiment and are not measured (some estimated from the similar trap specific parameters from [31]). The Rabi frequencies for analysis and precision trap differ only slightly and are listed only for the latter.. Note: This table and the axial frequency were adjusted after handing in the thesis. A sign error in the calculation script was fixed and the axial frequency was measured, resulting in new values. These values do not not change any of the arguments in this thesis, but are important for the measurements thereafter.

resonance gives a condition for Rabi frequency and excitation time

$$\Omega^2 \tau \begin{cases} \approx \frac{1}{\pi\chi(0)} \approx \begin{cases} \Delta\omega/\pi, & \text{electron spin transitions in the PT,} \\ \Delta\omega^2/\gamma, & \text{nuclear transitions in the PT,} \end{cases} \\ > \frac{1}{\pi\chi(0)} \approx \Delta\omega/\pi, & \text{in the AT.} \end{cases} \tag{3.24}$$

Owing to the much larger linewidth in the analysis trap, the last condition enforces the strongest requirement of radio-frequency field power and excitation time. As will be explained in the next section, only the electron spin transitions need to be driven in the analysis trap, for which the above evaluates to

$$B_{\text{RF}} \gtrapprox \frac{11}{\sqrt{\tau}} \text{ nT}\sqrt{\text{s}}. \tag{3.25}$$

3.5. Detecting spin-flip transitions and measurement scheme

The Continuous Stern-Gerlach Effect pioneered by Dehmelt [1] has been used for the detection of spin-flips inside Penning traps for the determination of the electron [2] and proton [5] g-factor as well as for several other magnetic moment Penning-trap experiments [32].

Using a ferromagnetic nickel ring electrode similar to that used for the proton g-factor experiment [5], a strong magnetic parabola field $B_2 \approx 110$ kT^2 is superimposed on the constant field. The resulting shift of the energies of the hyperfine splitting has been calculated in the

---

[2]This value was calculated using a FEM simulation with COMSOL Multiphysics® [33] to $B_2 \approx 87$ kT but later measured.

Hamiltonian given in Eq. (3.11). Effectively, the ion experiences a spin state dependant potential in the z-direction, which produces an additional restoring force on the ions axial motion. Let μ_i be the element of the matrix in the time dependant term of Eq. (3.11), then the axial motion $z(t)$ solves

$$\ddot{z}(t) + \omega_z^2 z(t) - \frac{2B_2\mu_i}{m} z(t) = 0, \tag{3.26}$$

where ω_z is axial frequency without any B_2. This shifts the effective axial frequency

$$\omega_{z,i} = \sqrt{\omega_z^2 - \frac{2B_2\mu_i}{m}} \approx \omega_z - \frac{B_2\mu_i}{m\omega_z}. \tag{3.27}$$

A jump in the monitored axial frequency indicates a spin-flip. For the nuclear and electron spin-flip transitions this amounts to $\Delta\omega_z = 43$ mHz and $\Delta\omega_z = 21.9$ Hz (also adjusted, see 3.2), respectively. While it is easy to resolve the frequency jump of 21.9 Hz, a jump of just a few mHz can not be measured with the planned setup and a different approach to detect the nuclear transitions will be used.

This experiment uses a double-trap technique [34]. For the electron spin transitions the scheme is identical to the one employed by other g-factor experiments. The spin state is first initialised in the analysis trap by driving and observing an electron spin-flip. Following an
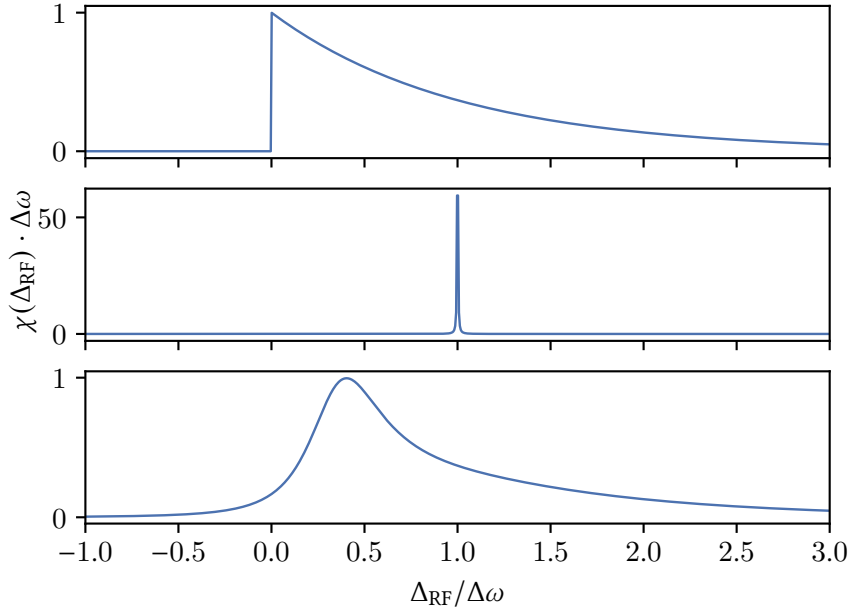

Figure 3.2: Line profiles in the analysis trap (top), nuclear transitions (middle) and electron spin transitions (bottom) in the precision trap. Note that the linewidths $\Delta\omega$ are very different for the electron and nuclear spin transitions and depend on the specific trap. For the general result given in Eq. (3.23) the series was found to converge for $n = 50$.
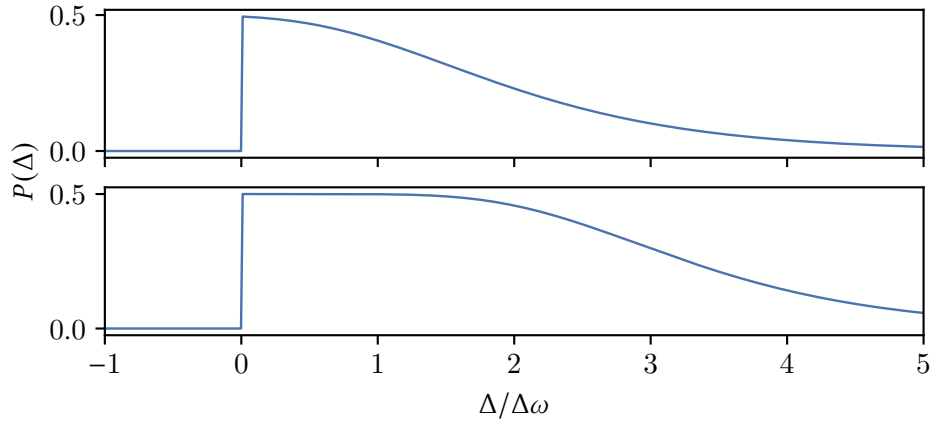
Figure 3.3: Spin-flip probability for the electron spin transitions inside the analysis trap. The top graph is for a Rabi frequency of $\Omega = 1000$ rad/s and the lower graph for $\Omega = 2000$ rad/s. The lower graph shows the broadening of the resonance that will be used for efficiently driving spin-flips at 50% in the analysis trap.

adiabatic transport, the transition is probed in a precision trap, which is optimized for a very small B_2 and linewidth. The ion is then transported back to the analysis trap, where the spin state is again read out by measuring the axial frequency shift following an excitation. If the direction of the observed frequency jumps in the analysis trap did not change, the spin-flip in the precision trap was successful. To efficiently drive the transition in the analysis trap at $P = 50\%$, the transition frequency only needs to be known on the order of $\omega/\Delta\omega \approx 10^{-5}$. Additionally, the spin-flip probability can be oversatured by increasing the microwave power, see Figure 3.3.

In order to detect nuclear spin-flips, a novel detection scheme will be used [35]. After an RF-pulse at the nuclear spin-flip frequency in the precision trap, a state selective RF-pulse resonant with an electron transition probes whether a nuclear spin-flip has occurred. The full measurement scheme for the nuclear transitions is shown in Figure 3.4.

A possible improvement to this scheme is the use of a technique called adiabatic fast passage [36], which enables spin-flip probabilities of up to 100%. By rapidly sweeping the frequency of the microwave field (or equivalently the static field) over the resonance of the spin-flip transition, the spin state is adiabatically changed. Applying this technique inside the analysis trap can drastically decrease the measurement time as only a single sweep determines the spin state.
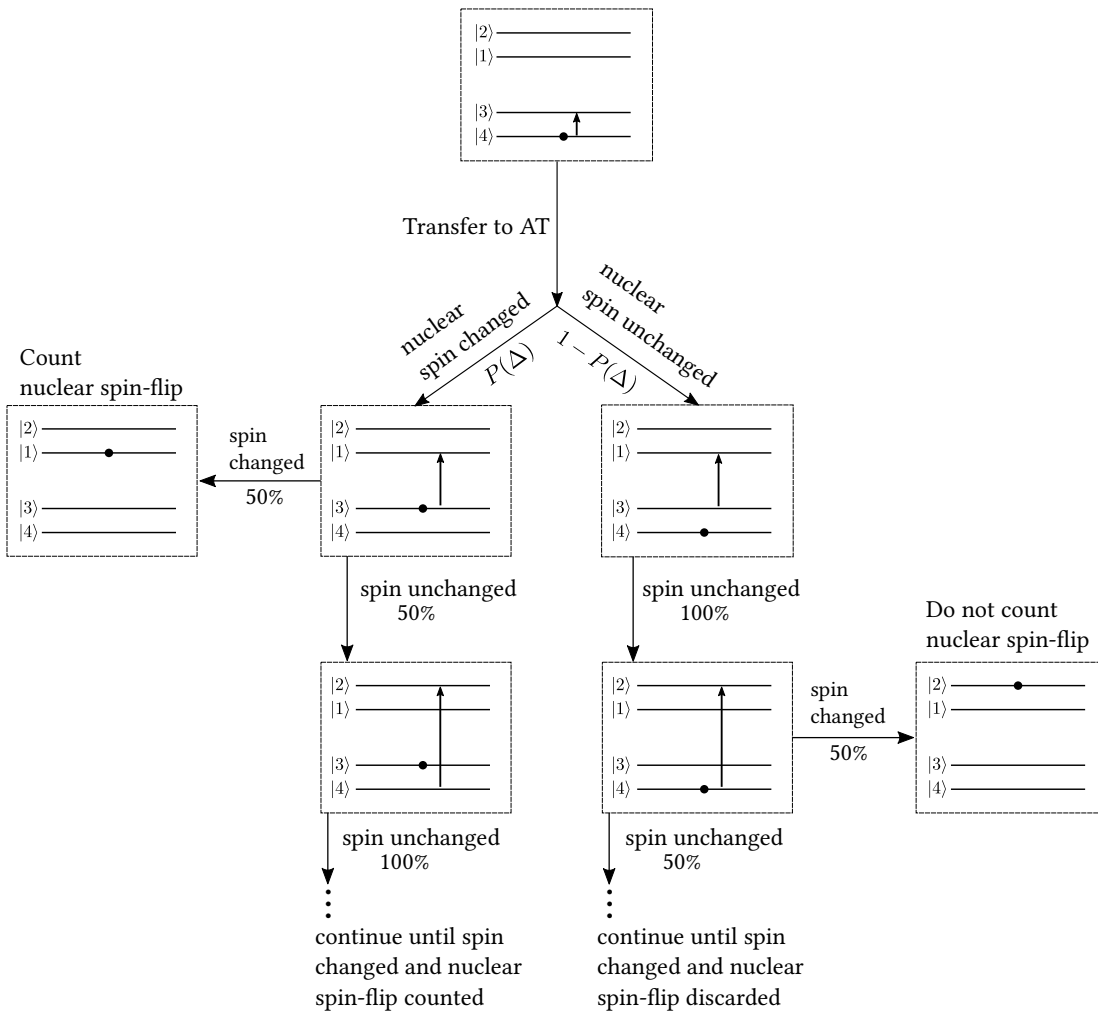
Figure 3.4: Nuclear spin-flip measurement scheme shown exemplarily for the 4.03 GHz $|4\rangle \rightarrow |3\rangle$ transition. After preparation in the analysis trap, the ion is transported to the precision trap, where the nuclear spin-flip is probed with microwaves detuned by Δ. The ion has switched its state with probability $P(\Delta)$. Back in the analysis trap, the two electron spin-flip transitions are alternately driven, while the axial frequency is monitored. This will eventually lead to a detected axial frequency jump, identifying whether the nuclear spin-flip in the precision trap was successful. Afterwards the ion is in the known state $|2\rangle$ or $|1\rangle$ and the other nuclear transition can be probed.

3.6. Determination of g_e, g_I and ΔE_{HFS}

The electron and nuclear g-factors g_e and g_I are connected to the spin magnetic moment through

$$g_e = \mu_e \frac{4m_e}{e\hbar}, \quad g_I = \mu_I \frac{4m_p}{e\hbar}, \tag{3.28}$$

respectively, where m_e and m_p are the mass of electron and proton and e is the electron charge. By measuring the transition frequencies ω_{ij} and the cyclotron frequency ω_c of $^3\text{He}^+$ in the Penning trap, compare Eq. (2.1) and Table 3.1, the g-factors are determined by

$$g_e = \frac{1}{\omega_c} \frac{m_e}{m_{^3\text{He}^+}} \left[(\omega_{24} - \omega_{12}) + \sqrt{(\omega_{24} - \omega_{34})^2 - (\omega_{12} + \omega_{34})^2} \right], \tag{3.29}$$

$$g_I = \frac{1}{\omega_c} \frac{m_p}{m_{^3\text{He}^+}} \left[(\omega_{12} - \omega_{24}) + \sqrt{(\omega_{24} - \omega_{34})^2 - (\omega_{12} + \omega_{34})^2} \right], \tag{3.30}$$

where $m_{^3\text{He}^+}$ is the mass of $^3\text{He}^+$. It should be noted that only three transitions enter the determination of the g-factors, as the fourth frequency can always be calculated from the other three. As masses enter as ratios only, the high accuracy values obtained in Penning traps, which measure masses relative to ^{12}C, can be used, see [37] for the electron, [38] for the proton and [39] for the ^3He mass. While for both g-factors the errors on the mass ratios and the cyclotron frequency enter equally, the errors from the measurement of the hyperfine transition frequencies enter more strongly in the nuclear g-factor g_I. This is due to the Zeeman effect in the intermediate regime. For higher magnetic fields the uncertainty of g_I and g_e resulting from the precision of the measured frequencies become equal. For the expected relative uncertainty of $\frac{\Delta\omega_{ij}}{\omega_{ij}} \sim 10^{-10}$ the relative errors on g_e and g_I obtained through standard propagation of errors are 10^{-10} and $2 \cdot 10^{-9}$, respectively.

The zero-field hyperfine splitting ΔE_{HFS} is the sum of the two nuclear transitions

$$\Delta E_{\text{HFS}} = \omega_{12} + \omega_{34}. \tag{3.31}$$

Owing to the effective magnetic shielding of the nuclear spin by the electron, the determination of the value of the zero-field hyperfine splitting is very insensitive to changes of the external magnetic field. If the magnetic field B fluctuates between measurement of ω_{12} and ω_{34} by the amount ΔB, the associated error on ΔE_{HFS} is suppressed by 2 orders of magnitude, i.e. $\frac{\Delta(\Delta E_{\text{HFS}})}{\Delta E_{\text{HFS}}} \sim 10^{-2} \frac{\Delta B}{B}$.

4. Microwave propagation in waveguides

To perform the electron spin-flip transitions, microwaves at ~ 150 GHz, see Table 3.2, need to be coupled into the Penning traps. To this end, it is crucial that enough radial magnetic microwave field is present at the ion's position, compare Eq. (3.24). In contrast to the lower frequency microwaves of around 4.5 GHz needed for the nuclear spin-flips, which can be coupled into the trap chamber with coaxial cables, the losses of microwaves at millimetre wavelengths are to high to efficiently transmit them with cables. This leaves hollow metal conductors (waveguides) as the only alternative.

Due to restrictions imposed by the setup, the transmission line can not be realised with a single long uniform waveguide, but requires non-uniform transition sections. In order to quantify the amount of microwave power that is transmitted through the experimental setup, a theoretical description of the electromagnetic fields inside the waveguide is needed. Additionally, the Penning trap itself constitutes a cylindrical hollow conductor and the same waveguide theory is needed to characterise the structure of the microwave field inside the stack of electrodes.

4.1. Transverse modes

The electromagnetic fields inside a waveguide are found by solving Maxwell's equations in free space [40]

$$\nabla \times \boldsymbol{E} + \partial_t \boldsymbol{B} = 0, \quad \nabla \cdot \boldsymbol{B} = 0,$$
$$\nabla \times \boldsymbol{B} - \frac{1}{c^2} \partial_t \boldsymbol{E} = 0, \quad \nabla \cdot \boldsymbol{E} = 0, \tag{4.1}$$

with the appropriate boundary conditions. Here, c denotes the speed of light inside the medium that fills the waveguide. Maxwell's equations in free space result in the wave equations

$$\frac{1}{c^2} \partial_t^2 \boldsymbol{E}(\boldsymbol{x}, t) = \Delta \boldsymbol{E}(\boldsymbol{x}, t), \quad \frac{1}{c^2} \partial_t^2 \boldsymbol{B}(\boldsymbol{x}, t) = \Delta \boldsymbol{B}(\boldsymbol{x}, t), \tag{4.2}$$

for the electric and magnetic field, respectively. The basis set of solutions to these equations without boundary conditions are plane waves with time and spatial dependence $e^{\pm i\omega t}$ and

$e^{i\boldsymbol{k}\cdot\boldsymbol{x}}$, respectively. Here, ω is the frequency of the electromagnetic wave and $\boldsymbol{k}$ the wavevector with $|\boldsymbol{k}|^2 = k^2 = \omega^2/c^2$. The boundary conditions imposed by the conducting walls of the waveguide constrain the vector space spanned by these free space solutions.

For the subsequent sections it will be assumed that the waveguide has an uniform cross-section. It is thus sensible to express the fields in terms of a component parallel to the axis of the waveguide (chosen to coincide with the z-axis) and a transverse component

$$\boldsymbol{E} = \boldsymbol{E}_T + E_z \boldsymbol{e}_z, \quad \boldsymbol{B} = \boldsymbol{B}_T + B_z \boldsymbol{e}_z. \tag{4.3}$$

The time dependence of the fundamental solutions of the wave equations inside the waveguide, called modes, are not constrained by the geometry and therefore equal to $e^{\pm i\omega t}$. The modes further retain the z-dependence $e^{\pm i k_z z}$ of the free space solution due to the translational symmetry of the uniform waveguide. These considerations lead to wave equations for the z-components of the fields [41]

$$\left(\Delta_T + k_T^2\right) E_z = 0, \quad \left(\Delta_T + k_T^2\right) B_z = 0, \tag{4.4}$$

where $\Delta_T = \Delta - \partial_z^2$ is the transverse part of the Laplace operator and $k_T^2 = k^2 - k_z^2$ is the transverse wavevector. Maxwell's equations (4.1) relate the transverse fields to the axial fields

$$\begin{aligned}
k_T^2 \boldsymbol{E}_T &= -i\omega \boldsymbol{e}_z \times \nabla_T B_z + \partial_z \nabla_T E_z, \\
k_T^2 \boldsymbol{B}_T &= i\frac{\omega}{c^2} \boldsymbol{e}_z \times \nabla_T E_z + \partial_z \nabla_T B_z.
\end{aligned} \tag{4.5}$$

On the surface of a perfectly conducting wall, the components of the electric field tangential to it and the components of the magnetic field normal to it vanish. Therefore, the axial component E_z of the electric field and the transverse component $\boldsymbol{B}_T$ of the magnetic field vanish on the surface. The condition on $\boldsymbol{B}_T$ can be transformed with Eq. (4.5) resulting in

$$E_z|_S = 0, \quad \partial_n B_z|_S = 0 \tag{4.6}$$

for the z-components of the electric and magnetic fields on the walls of the waveguide. Because these boundary condition can be fulfilled separately and E_z and B_z solve independent differential equations, there exist two distinct types of modes:

Transverse magnetic (TM) waves have no axial magnetic field and obey the Dirichlet boundary condition $E_z|_w = 0$.

Transverse electric (TE) waves have no axial electric field and obey the Neumann boundary condition $\partial_n B_z|_w = 0$.

Solving Eq. (4.4) under the boundary conditions of Eq. (4.6) for a waveguide with a given cross-section results in the axial fields of the TE and TM modes. The transverse components can be calculated using Eq. (4.5). Because either E_z or B_z are zero for the TE and TM modes, the two equations in Eq. (4.5) can be used to directly connect the transverse electric and magnetic field through

$$\boldsymbol{B}_T = \pm \frac{\mu_0}{Z} \boldsymbol{e}_z \times \boldsymbol{E}_T, ^1 \tag{4.7}$$

---

[1] The $\pm$ sign stems from the spatial z-derivative.

where μ_0 is the vacuum permeability and Z is called the wave impedance which is defined by

$$Z = Z_0 \frac{k}{k_z}, \text{ for TE waves,}$$

$$Z = Z_0 \frac{k_z}{k}, \text{ for TM waves.}$$

(4.8)

Here, $Z_0 = \mu_0 c$ is the impedance of the vacuum. The wave impedance, like the usual impedance, connects currents ($\boldsymbol{B}$) and voltages ($\boldsymbol{E}$) inside a conductor.

4.2. Circular waveguide modes

The mode structure in a waveguide with circular cross-section and radius R can be calculated analytically. First, the axial wave equation (4.4) needs to be solved in cylindrical coordinates $(x, y, z) = (\rho \cos(\varphi), \rho \sin(\varphi), z)$. This calculation, which is the same for the TE (B_z) and TM (E_z) waves, results in the fields [41] (omitting the z-dependence)

$$B_z(\rho, \varphi) = B_0 J_m(k_T \rho) e^{\pm i m \varphi}, \text{ for TE waves,}$$

$$E_z(\rho, \varphi) = E_0 J_m(k_T \rho) e^{\pm i m \varphi}, \text{ for TM waves,}$$

(4.9)

where m is the azimuthal wavenumber, J_m are the Bessel functions of the first kind and E_0, B_0 specify the absolute amplitude of the waves. Applying the boundary conditions given in Eq. (4.6) to the above fields restricts the transverse wavevector k_T according to

$$k_{T,mn} = \frac{\beta_{mn}}{R}, \quad J'_m(\beta_{mn}) = 0, \text{ for TE waves,}$$

$$k_{T,mn} = \frac{\alpha_{mn}}{R}, \quad J_m(\alpha_{mn}) = 0, \text{ for TM waves,}$$

(4.10)

where J'_m is the first derivative of the Bessel function and $n \geq 1$ the radial wavenumber, which specifies the n'th zero of the Bessel function (derivative).

The quantisation is easily understood: The m-quantum number ensures that the wave is symmetric under a rotation about the z-axis by an angle of 2π and, due to the boundary conditions, the fields need to be zero (TM) or extremal (TE) at $\rho = R$ and thus have n wave crests (throughs) in the radial direction.

4.3. Cutoff frequencies and ohmic losses

Since for any kind of waveguide cross-section there are restrictions on two of the three spatial directions, a quantisation of the transverse wavenumber $k_{T,mn}$ with two mode numbers m and n occurs. Given the frequency of the microwave field ω, the total wavevector norm $k = \omega/c$ is divided into a transverse and an axial component. The transverse component is fixed by the mode of the field, which leaves the axial component with

$$k_z = \sqrt{\frac{\omega^2}{c^2} - k_T^2}.$$

(4.11)

For small enough values of ω the propagation in the z-direction is exponentially damped as k_z becomes imaginary. This defines the cutoff frequency

$$v_c = \frac{c}{2\pi} k_{T,mn},\tag{4.12}$$

below which propagation of the microwaves inside the waveguide is not possible. The mode with the smallest cutoff frequency is called the fundamental or dominant mode of the waveguide. Modes that have an imaginary axial wavevector component are evanescent modes.

Mode	Cutoff frequency	Fundamental mode cutoff
TE circular	$v_c = \frac{c}{2\pi} \frac{\beta_{mn}}{R}$	$v_{c,\mathrm{TE}_{11}} \approx 0.586 \frac{c}{2R}, \quad \lambda_{c,\mathrm{TE}_{11}} \approx 1.706 \cdot 2R$
TM circular	$v_c = \frac{c}{2\pi} \frac{\alpha_{mn}}{R}$	
TE rectangular	$v_c = \frac{c}{2}\sqrt{\frac{m^2}{a^2} + \frac{n^2}{b^2}}$	$v_{c,\mathrm{TE}_{10}} = 0.5\frac{c}{a}, \quad \lambda_{c,\mathrm{TE}_{11}} = 2 \cdot a$
TM rectangular	$v_c = \frac{c}{2}\sqrt{\frac{m^2}{a^2} + \frac{n^2}{b^2}}$	

Table 4.1: Cutoff frequencies v_c for circular waveguides with radius R and rectangular waveguides [41] with side lengths $a > b$ and cutoff frequency and wavelength λ_c of the corresponding fundamental mode. For the circular waveguide $m \geq 0, n \geq 1$ and for the rectangular waveguide n and m cannot both be zero for the TE modes and $n \geq 1, m \geq 1$ for the TM modes.

Table 4.1 lists the cutoff frequencies for circular and rectangular waveguides and Figure 4.1 shows the spatial structure of the fundamental modes. In rectangular waveguides the largest possible wavelength is exactly twice the side length a, whereas in circular waveguides the largest wavelength is slightly smaller than twice the diameter.

To include ohmic losses on the waveguide walls due to finite surface conductivity an imaginary term is added to the axial wavenumber k_z^{mn} leading to exponential damping of the wave amplitude. For circular waveguides a calculation gives [42]

$$\begin{aligned} k_{z,mn} &\to k_{z,mn} + i\sqrt{\frac{\pi\epsilon_0 v}{R^2\sigma\left(1 - \frac{v_c^2}{v^2}\right)}}, \quad \text{for TM modes,} \\[2em] k_{z,mn} &\to k_{z,mn} + i\sqrt{\frac{\pi\epsilon_0 v}{R^2\sigma\left(1 - \frac{v_c^2}{v^2}\right)}}\left(\frac{v_c^2}{v^2} + \frac{m^2}{\beta_{mn}^2 - m^2}\right), \quad \text{for TE modes,} \end{aligned}\tag{4.13}$$

where σ is the conductivity of the material of the waveguide and $v > v_c$ the frequency. The losses reduce with increasing radius R of the waveguide and increase with higher mode numbers m, n for $m \geq 1$.

Standard waveguides are usually used for frequencies that only allow the fundamental mode to propagate. The structure of the fields inside these waveguides is thus easy to calculate. Except from the losses on the waveguide walls, the fundamental mode does not lose any power.
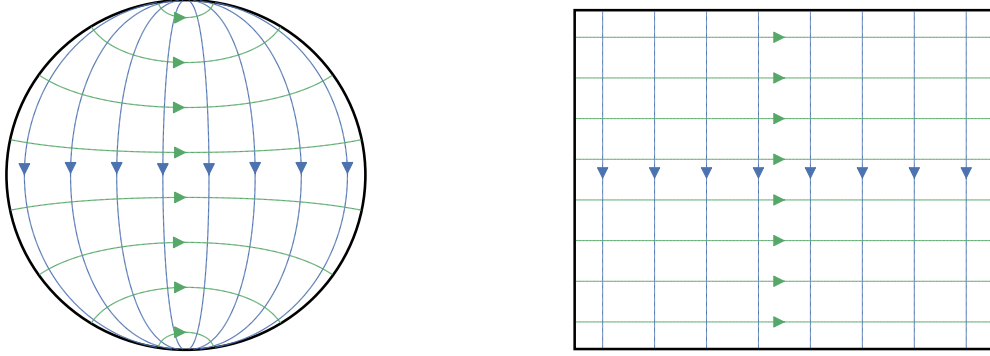
Figure 4.1: Transverse field structures for the fundamental TE_{11} mode in circular (left) and the fundamental TE_{01} mode in rectangular (right) waveguides. Equipotential lines of the magnetic and electric field are coloured blue and green, respectively.

4.4. Scattering matrix of the non-uniform circular waveguide

As the ion oscillates on the symmetry axis of a waveguide, namely the cylindrical trap itself, a transverse field component at $\rho = 0$ is needed. Fortunately, as shown in 4.1, the fundamental TE_{11} mode provides just that. Thus, starting with the power of the fundamental mode at the microwave generator, the transmission of the TE_{11} into the setup needs to be calculated.

Since the experimental setup includes circular waveguide sections with varying diameter, calculating the transmission through such a non-uniform section is needed. This is possible with finite element calculations or using a numerical mode-matching technique [43]. In order to have a tool for analysing non-uniform circular waveguide sections and to have an independent validation of the finite element calculations the mode matching technique is described in this section and an algorithm for computing the transmission is presented. The more mathematical details are worked out in Appendix A.

Figure 4.2 shows two circular waveguides of different radii connected via a circular waveguide with an arbitrary profile. The transverse electric $E_T^{l,r}(x)$ and magnetic $B_T^{l,r}(x)$ fields on the left (l) and right (r) side of the non-uniform waveguide can be written as a sum over circular waveguides modes and both negative and positive z-direction:

$$E_T^{l,r}(x) = \sum_n \left(I_n^{l,r} e^{\mp i k_z z} + O_n^{l,r} e^{\pm i k_z z} \right) e_n^{l,r}(x, y),$$

$$B_T^{l,r}(x) = \sum_n \pm \frac{\mu_0}{Z_n^{l,r}} \left(I_n^{l,r} e^{\mp i k_z z} - O_n^{l,r} e^{\pm i k_z z} \right) h_n^{l,r}(x, y).$$

$$(4.14)$$

Here, I is the vector of incoming (relative to the center section) electric field wave amplitudes and O the vector of outgoing amplitudes. The magnetic field amplitudes are related to the electric field through the wave impedance Z and Eq. (4.7). The mode vectors $e_n^{l,r}(x, y)$ and
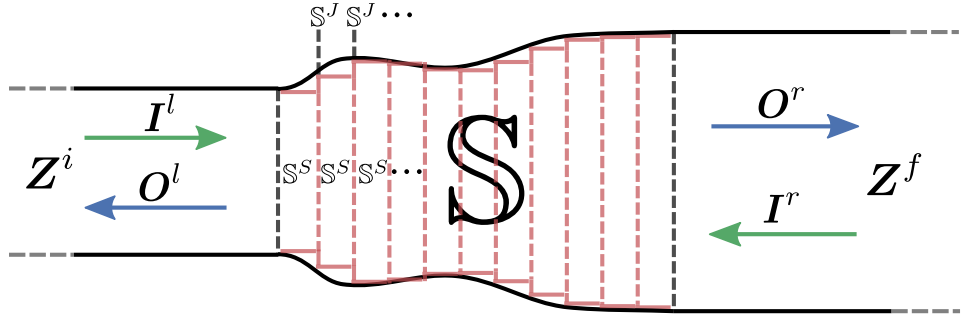
Figure 4.2: Cross-section of two sections of uniform circular waveguides connected by another circular waveguide with an arbitrary profile. The red lines indicate the discretisation of the problem. For a detailed description of the variables see text.

$h_n^{l,r}(x,y) = e_z \times e_n^{l,r}(x,y)$ contain the transverse spatial dependence of the specific mode n. Eq. (4.14) can also be interpreted as the electromagnetic field being written as a sum of components of a vector multiplied by the basis functions $e_n^{l,r}(x,y)$ and $h_n^{l,r}(x,y)$.

Using the definition of the scattering matrix (S-matrix)

$$\begin{pmatrix} O^l \\ O^r \end{pmatrix} = \mathbb{S} \begin{pmatrix} I^l \\ I^r \end{pmatrix} = \begin{pmatrix} \mathbb{S}_{11} & \mathbb{S}_{12} \\ \mathbb{S}_{21} & \mathbb{S}_{22} \end{pmatrix} \begin{pmatrix} I^l \\ I^r \end{pmatrix}, \tag{4.15}$$

the in- and outgoing amplitudes can be connected. The S-matrix completely describes transmission and reflections inside the arbitrary shaped waveguide piece. As an example, the diagonal entry $(\mathbb{S}_{21})_{nn}$ corresponding to $n = \text{TE}_{11}$ is considered. Given unity input of the TE_{11} mode on the left side, its value is the output amplitude of the TE_{11} mode on the right side. Off-diagonal entries $(\mathbb{S}_{21})_{mn}$ give conversion between modes, for example, given unity input amplitude of the $n = \text{TE}_{11}$ mode its value is the amplitude of the $m = \text{TE}_{12}$ mode at the output. If both input and output have radii such that they support only the fundamental mode, the additional modes created through mode conversion decay very fast. Thus, there are effectively only diagonal terms in the submatrices of the S-matrix and it is fully described by reflection and transmission of the fundamental mode.

The amplitudes associated with the scattering matrix are the electric field amplitudes. In analogy to the power inside an electrical conductor given by the voltage and the resistance, the power of a waveguide mode is proportional to the electric field amplitude squared divided by the wave impedance [44]. The transmitted power P_{mn} in mode m at the output given unity input power in mode n is calculated by multiplying the square of $(\mathbb{S}_{21})_{mn}$ with the wave impedances of the initial and final waveguide geometry:

$$P_{mn} = |(\mathbb{S}_{21})_{mn}|^2 \frac{Z_n^i}{Z_m^f}. \tag{4.16}$$

The mode-matching technique calculates the scattering matrix of a non-uniform waveguide by discretising the arbitrary shaped waveguide into small pieces of uniform waveguide and

junctions between those, see Figure 4.2. Both junctions and uniform waveguide sections can be described by a corresponding scattering matrix. The straight section scattering matrix $\mathbb{S}^S$ is straightforward to calculate, as the waves acquire only a phase given by the axial wavenumber k_z^n and the length of the section δz:

$$\mathbb{S}_{12}^S = \mathbb{S}_{21}^{S\dagger} = \mathrm{diag}\left(e^{ik_z^n \delta z}\right),$$
$$\mathbb{S}_{11}^S = \mathbb{S}_{22}^S = 0. \tag{4.17}$$

By requiring continuity of the transverse fields at the junctions between the uniform sections there is mode conversion. Mathematically, this can be thought of as a change of basis from one side of the junction to the other, as the basis functions $\boldsymbol{e}_n^{l,r}(x,y)$ and $\boldsymbol{h}_n^{l,r}(x,y)$ depend on the radius. The overlap between these basis functions, i.e. the integral of their product over the common cross-section, quantifies the mode coupling. Its easy to see that the overlap between circular modes of different azimuthal mode number m is zero, compare Eq. (4.9), because the integral over the angle φ always gives a vanishing result. These considerations result in the scattering matrix of the junction $\mathbb{S}^J$, given in Eq. (A.12).

Given two waveguide components with S-matrix $\mathbb{S}^1$ and $\mathbb{S}^2$, the composite S-matrix $\mathbb{S}$ is calculated by cascading the two matrices [43]

$$\mathbb{S}_{11} = \mathbb{S}_{11}^1 + \mathbb{S}_{12}^1 \mathbb{S}_{11}^2 \mathbb{E} \mathbb{S}_{21}^1,$$
$$\mathbb{S}_{12} = \mathbb{S}_{12}^1 \left(\mathbb{I} + \mathbb{S}_{11}^2 \mathbb{E} \mathbb{S}_{22}^1\right) \mathbb{S}_{12}^2,$$
$$\mathbb{S}_{21} = \mathbb{S}_{21}^2 \mathbb{E} \mathbb{S}_{21}^1,$$
$$\mathbb{S}_{22} = \mathbb{S}_{22}^2 + \mathbb{S}_{21}^2 \mathbb{E} \mathbb{S}_{22}^1 \mathbb{S}_{12}^2, \tag{4.18}$$

with $\mathbb{E}$ being a matrix inverse

$$\mathbb{E} = \left(\mathbb{I} - \mathbb{S}_{22}^1 \mathbb{S}_{11}^2\right)^{-1}. \tag{4.19}$$

The total scattering matrix for the waveguide for different microwave frequencies is then calculated as follows:

1. **Discretisation:** Discretise the radial profile of the waveguide, see Figure 4.2, assign the number of modes via Eq. (A.13) and calculate the frequency independent mode coupling matrices with Eqs. (A.16, A.17, A.18) for each junction.

2. **For each frequency ν and at each junction:** Calculate the axial wavenumbers given in Eq. (4.13) to include ohmic losses, the impedances $Z(\nu)$, Eq. (4.7), and the scattering matrix $\mathbb{S}(\nu)$ of the junction, Eq. (A.12). Cascade the scattering matrix with the total scattering matrix of all preceding sections, Eq. (4.18), and with the scattering matrix of the following straight section, Eq. (4.17).

3. **For each frequency:** With the radii of the input and output of the waveguide calculate the transmitted power according to Eq. (4.16).

Using the programming language C++ and the linear algebra library Eigen [45], a program that implements this algorithm was developed. It takes the discretised radial profile together with conductivities as inputs and calculates the transmission of the TE_{11} mode.

5. Design of the waveguide for the microwave transmission line

In order to excite electron spin-flips inside the apparatus, microwaves at a frequency of about 150 GHz, corresponding to a wavelength of ∼ 2 mm, need to be coupled into the Penning traps. Compared to the much lower frequency microwaves of the nuclear spin-flip at ∼ 4.5 GHz, which can be coupled into the trap chamber with coaxial cables, the losses of microwaves at millimetre wavelengths are to high to efficiently transmit them with cables, leaving waveguides as the only alternative.

In terms of construction, a transmission line using waveguides poses considerably more problems than using conventional cables. As can be seen from the experimental setup shown in Figure 5.1, the total length the microwaves need to be transmitted inside the experiment is larger than 1.5 m. Additionally, there are two vacuum transitions that require the hollow conductor to be interrupted by glass windows.

The frequencies required are part of the D-band, for which the rectangular waveguide standard WR6 with dimensions of 1.651×0.826 mm is used if transmission of microwaves in a waveguide with only a single propagating mode is required. Ideally these waveguides are made of gold plated copper, which results in losses of the order of 10 dB/m [47]. There are a few reasons making standard WR6 waveguides impractical for usage in this experiment. Copper waveguides connecting the high temperature part at the top of the experiment with the cryogenic trap chamber would result in a large heat load, requiring higher consumption of liquid helium by the cryostat. In addition, due to the very small dimensions, manufacturing WR6 waveguides at the required lengths is not easy and the maximum length found to be commercially available was 50 cm. Custom made parts needed for the vacuum transition sections and connections to the Penning traps would need to be made at the workshop of the MPIK. Having one end of the custom made part at the very small size of the single mode waveguide would place some impractical limits on the dimensions machinable. For example, the length of such parts could not exceed a few centimetres.

Transferring microwaves over distances of the order of a few meters is also possible by using oversized waveguides, i.e. waveguides that allow a multitude of modes to propagate [48]. In principle, larger waveguides have lower ohmic losses than single mode waveguides, compare Eq. (4.13), allowing for the usage of worse conducting materials like stainless steel. Using
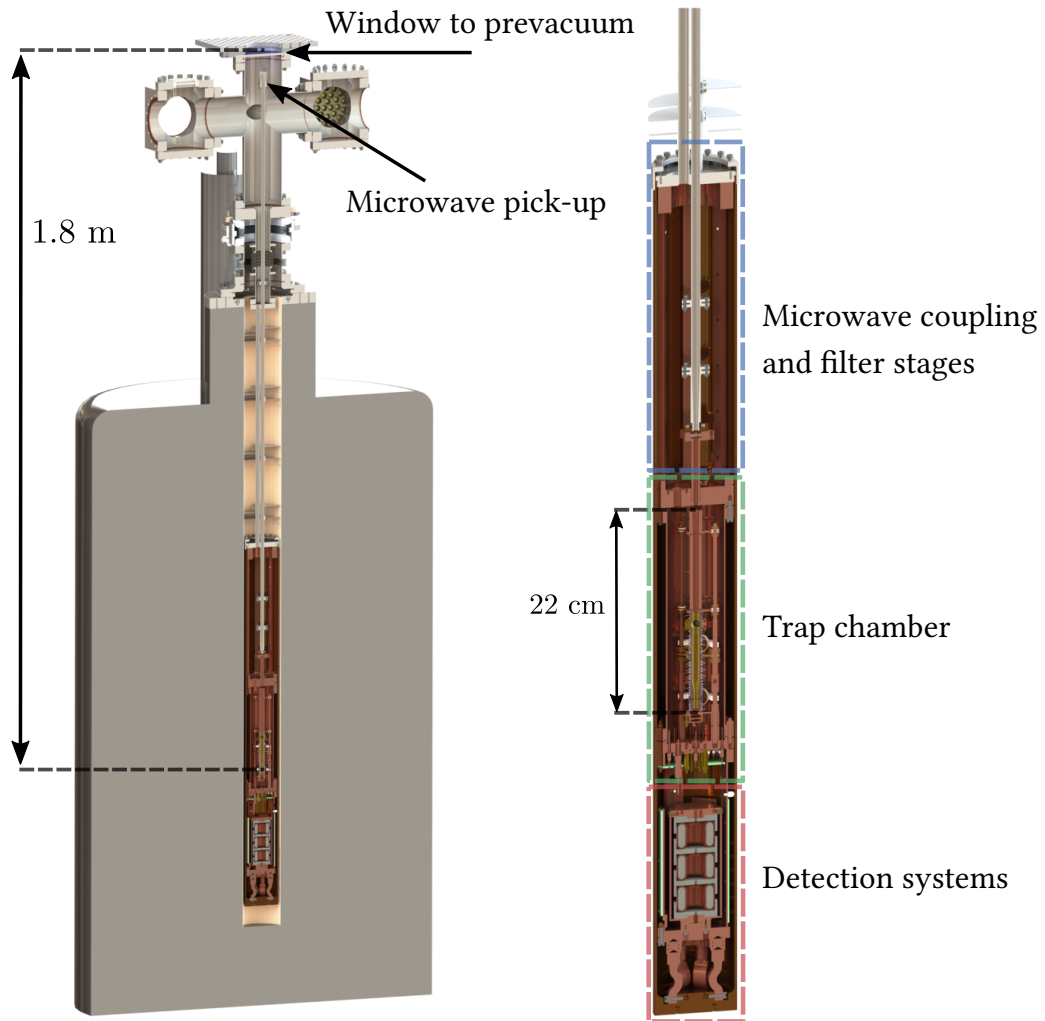
Figure 5.1: CAD model of the experimental setup for the ^{3}He$^+$ hyperfine structure measurement. For a description of the parts for the microwave injection see text. On the right hand side a close up shows the prevacuum chamber [35]. Inside the blue marked region the voltage bias lines for the trap electrodes and the amplifiers are filtered using LC circuits. The green marked region shows the trap chamber. The ions are produced inside this chamber using a glass sphere containing ^{3}He as a source and a field emission point for ionisation, see [46] for more details. Inside the red marked region the detection system with the superconducting coils and the cryogenic amplifiers are located.

easily available stainless steel pipes with a radius of 4 mm as the oversized waveguide reduces the heat load drastically and enables the workshop to manufacture the additional parts more easily. The main challenge presenting itself with oversized waveguides is mode conversion at transition sections, see Section 4.4. In contrast to a single mode waveguide where any modes

beside the fundamental mode are evanescent, here the modes converted at transition sections can propagate in regions where the radius is large enough. Cavity like resonances due to trapping of modes inside these regions can cause considerable loss of power in the fundamental mode.

In the following, the requirements for the microwave injection in terms of power transmission are worked out. Then the viability of using oversized waveguides is further investigated. To this end the numerical method of Section 4.4 and finite element calculations with COMSOL are used to optimise different transition sections for maximum transmission. This chapter concludes with an estimate for the total expected losses.

5.1. Required performance of the microwave injection

The waveguide injection system needs to transmit microwaves at the four electron spin-flip transition frequencies listed in Table 3.2. As explained at the end of Section 3.4, the frequencies inside the analysis trap pose the strongest requirement in terms of RF-field amplitude.

Because the ions oscillate on the symmetry axis of a waveguide, namely the cylindrical trap itself, driving spin-flip transitions requires a transverse magnetic field component at $\rho = 0$. Fortunately, as shown in 4.1, the fundamental TE_{11} mode provides just that. Thus, the problem of obtaining a large enough RF-field amplitude at the ions position, translates to being able to transmit enough power of the TE_{11} mode into the analysis trap. Given a required transverse magnetic field on axis B_{RF}, the corresponding power inside the TE_{11} mode is

$$P = \frac{2\pi c}{\mu_0} \frac{k}{k_z} \frac{1}{k_T^2} J_m^2(\beta_{11})(\beta_{11}^2 - 1)B_{RF}^2, \qquad (5.1)$$

with the definitions elaborated in Chapter 4. The derivation here relies on [44] and the explicit form of the normalisation of the TE_{11} mode found in Appendix A.2.

Allowing for an excitation time of $\tau = 10$ s, the needed magnetic field given by condition Eq. (3.25) is $B_{RF} \approx 3.5$ nT. Together with a radius of $r_{AT} = 1.8$ mm, the power injected into the analysis trap has to be

$$P > 15 \text{ nW} \approx -48 \text{ dBm}. \qquad (5.2)$$

In contrast, the field required inside the precision trap due to the condition given in Eq. (3.24) is only ~ 9 pT. Again using Eq. (5.1) and $r_{PT} = 3.5$ mm, this gives the much weaker condition of $P > -95$ dBm. The output power of the acquired *Signal Generator Extension Module WR6.5SGX* from *VDI* producing the microwaves is advertised to be ~ 5 dBm [49], limiting the allowed total losses of the microwave injection to a maximum of 53 dB.

5.2. FEM calculations

As an alternative to the mode matching approach presented in Section 4.4, finite element method (FEM) calculations with COMSOL Multiphysics® [33] are used to compute microwave transmissions and field structures. Additionally, FEM calculations also allow for modelling of free space regions as opposed to the mode matching technique. For this purpose the RF Module

of COMSOL is used to solve for the structure of the microwaves, given an input mode. The calculation mesh needs to be about on order of magnitude smaller than the wavelength of the microwaves. As the structures on which the finite element method will be applied are generally much larger than a wavelength, i.e. oversized, models that use a full three dimensional structure can not be solved in a reasonable amount of time. This restricts models to have an axisymmetric geometry which reduces them effectively to two dimensions.

In the following, the setup procedure for a calculation in COMSOL is described briefly:

1. **Model definition:** A *2D axisymmetric* model using the *Electromagnetic Waves, Frequency Domain* physics interface and a *Frequency Domain* study is set up.

2. **Geometry:** The geometry of the waveguide problem is set up. In order to model free space transitions, a circle with appropriate radius (condition explained later in the last step) is drawn around the section. Materials for the boundaries and domains are set up.

3. **Physics definitions:** In order to use a TE_{11} wave as the input field, the azimuthal mode number is set to $m = 1$. On metal surfaces the *Impedance Boundary Condition* is used to account for imperfectly conducting surfaces [50]. This condition is a more general version of the one given for perfectly conducting walls in Eq. (4.6). At the free space boundaries the electromagnetic field should ideally pass through and be lost into free space. This is approximately realised using the *Scattering Boundary Condition* [51]. The input surface boundary is defined as a *Circular Port* [52] with radial mode number $n = 1$ and a given input power. This sets the boundary to the field structure of the TE_{11} mode. In general, the field at the surface is a superposition of all modes that can propagate, compare Eq. (4.11). Therefore, additional *Circular Ports* without excitation are set up for all allowed modes at both input and output boundaries.

4. **Mesh:** The mesh size is a parameter for which generally a convergence study is necessary. Here the mesh maximum grid spacing of about a fifth of the wavelength showed convergent results. If more accurate results are needed on axis, a separate mesh with closer spacing can be used there.

5. **Study and results:** The model is solved with the desired range of frequencies. It is useful to add a *Power flow, time average* arrow surface to the solution of magnetic/electric field to see whether the power in the free space regions exits the circle at right angles (and is not reflected).

See also Figure 5.6 for an example showing a geometry and the corresponding boundary conditions.

As a result, the S-Matrix parameters of the waveguide section and the structure of the fields inside the waveguide are given. The values of the fields are time averaged values, meaning that the time evolution of the individual field components is governed just by an oscillation at the frequency of the microwaves.

5.3. Oversized waveguides

Employing oversized circular waveguides for low loss transmission of millimetre microwaves is an established technique and has been investigated thoroughly [48, 53, 54]. A major problem of oversized waveguides are trapped modes, as illustrated in Figure 5.2. Essentially modes are trapped in the region Δz in which they are able to propagate, i.e. where the axial wavevector Eq. (4.11) is real. For specific frequencies, the phase that builds up in the region Δz due to the axial propagation with $\exp(ik_z z)$ is exactly a multiple of 2π leading to constructive interference and power being resonantly transferred to this mode. These cavity resonances lead to sharp drops in the transmission of the fundamental mode [48].

In a waveguide with a finite conductivity, the build-up of amplitude in a reflected mode is dampened, compare Eq. (4.13), leading effectively to cavity losses. Additionally, the losses for the individual mode decrease with ν/ν_c, resulting in the fundamental mode to have the lowest losses. Therefore, it is expected that these resonances vanish, if the oversized section is long enough.

In the following sections, all calculations including the materials copper, stainless steel and gold use conductivity values of $\sigma_{\mathrm{Cu}} = 5.98 \cdot 10^7$ S/m, $\sigma_{\mathrm{Au}} = 4.25 \cdot 10^7$ S/m and $\sigma_{\mathrm{SS}} = 1.33 \cdot 10^6$ S/m, respectively [55]. The surface quality of the materials is also relevant for the transmission of microwaves. This is most relevant for the 1.5 m long stainless steel pipe, but due to the very good surface roughness of only 0.6 μm achieved with electropolishing, which is less than the skin depth of around 1 μm, this effect can be neglected [56].
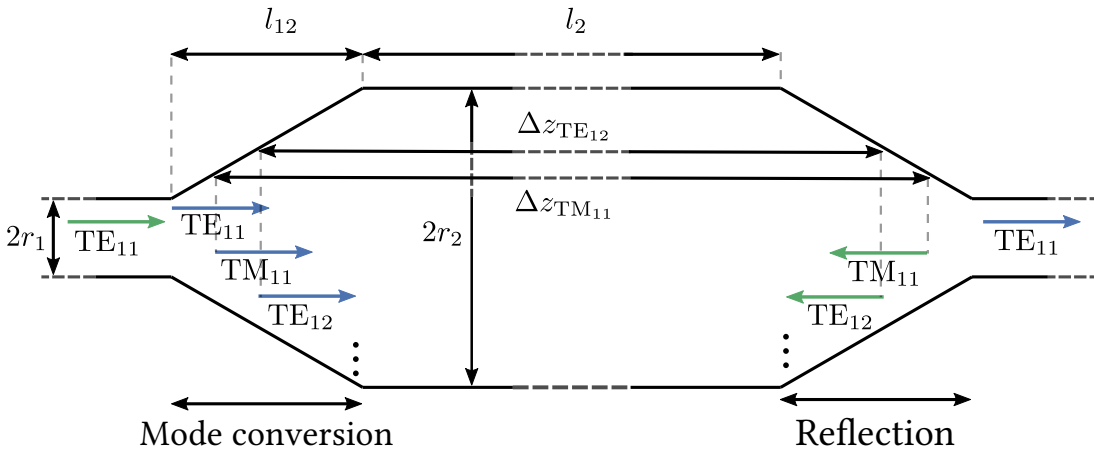

Figure 5.2: Illustration of the formation of trapped modes inside an oversized waveguide connected to single mode waveguides at both ends. With increasing radius, more modes can propagate and are formed through mode conversion. On the right side, these additional modes are reflected as the radius decreases below the value needed for the mode to propagate.

5.3.1. Comparison of FEM calculations and mode matching technique

A waveguide section as shown in Figure 5.2 is now used to compare the TE_{11} transmission calculated with the mode matching method and the FEM calculations. For this, values of $r_1 = 700$ μm for the single mode section and $r_2 = 1.2$ mm for the oversized section are used. The linear transition section connecting them is $l_{12} = 5$ mm long. For all sections copper is used as the material.

Figure 5.3 clearly shows an excellent agreement between the two methods, with a maximum relative deviation of just a few times per 10^{-3}. This confirms that the FEM calculations are properly set up and is a good check for the correctness of transmission calculations using
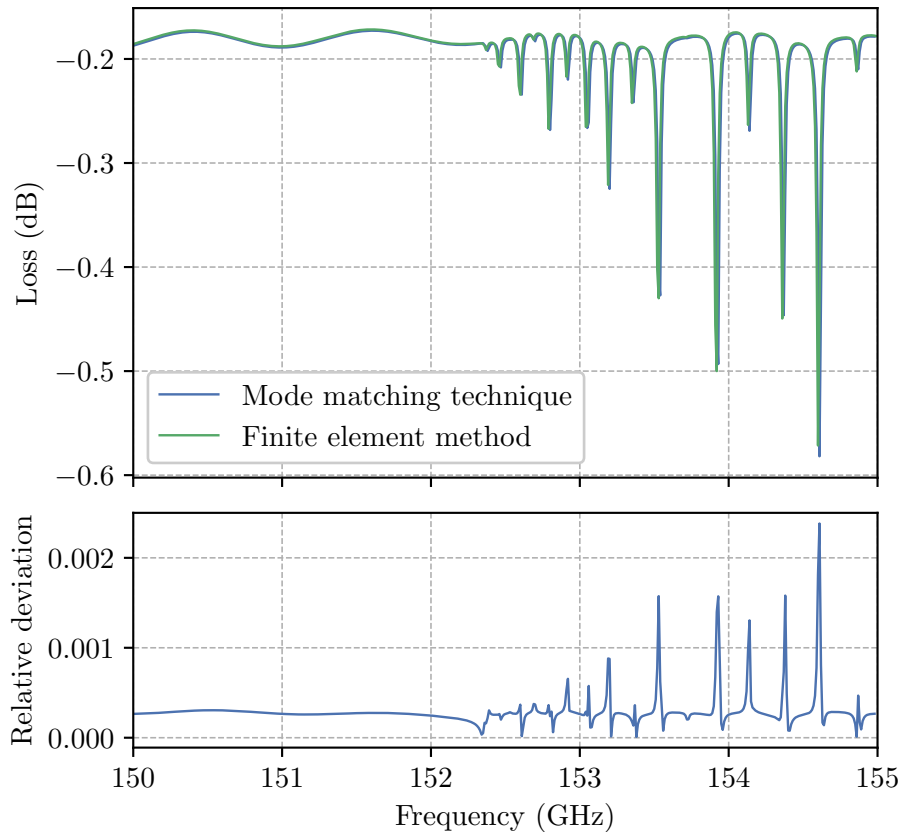

Figure 5.3: Top: TE_{11} transmission calculated by the mode matching method (blue line) and the COMSOL calculations (green line). The geometry is described in the text. For the mode matching method the transition section was divided into 100 discrete step junctions and an initial number of $n = 5$ modes was used for the single mode section. The FEM computation took around 15 minutes to finish, whereas the mode matching algorithm completed in just 3 minutes. **Bottom:** Relative deviation of the transmission calculated by the two methods, showing that both methods are in excellent agreement.

the finite element method that are not possible with the mode matching technique. A major advantage of the mode matching method is the much faster computation time, allowing for fast checks and parameter adjustments of simple geometries. While the FEM calculation needs to solve Maxwell's equations at every point of the two-dimensional geometry, the numerical algorithm directly computes the transmission. Additionally, increasing the length of oversized section does not increase the computation time of the mode matching algorithm, as any straight section just corresponds to a single scattering matrix that needs to be cascaded.

Figure 5.3 also shows the features appearing due to trapped modes. For frequencies higher than ~ 152 GHz the TM_{11} mode is allowed to propagate, leading to equally spaced resonances due to the reflection of the mode at the transition section. As the damping of microwaves in the TM_{11} mode decreases with increasing frequency, compare Eq. (4.13), the resonances increase.

5.3.2. Damping of resonances

Using the mode matching method, the damping of trapped mode resonances is investigated with the geometry described in the previous section and increasing length of the oversized waveguide. Figure 5.4 shows that with increasing the oversized waveguide length, the spacing between the resonances decreases, but their depth also decreases relative to the mean transmission.

The shape of the transition section determines the amount of mode conversion from the fundamental mode to the other modes. Generally, mode conversion is higher for a shorter transi-
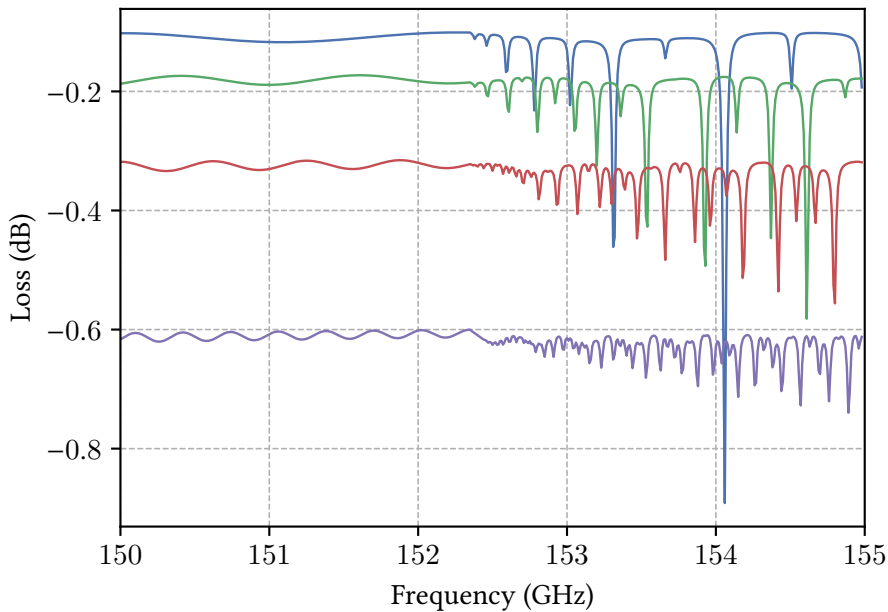

Figure 5.4: Damping of trapped mode resonances. Geometry described in Section 5.3.1. The length of the oversized waveguide section is increased by factors of 2 starting from $l_2 = 5$ cm (blue line) and ending at $l_2 = 40$ cm (purple line).
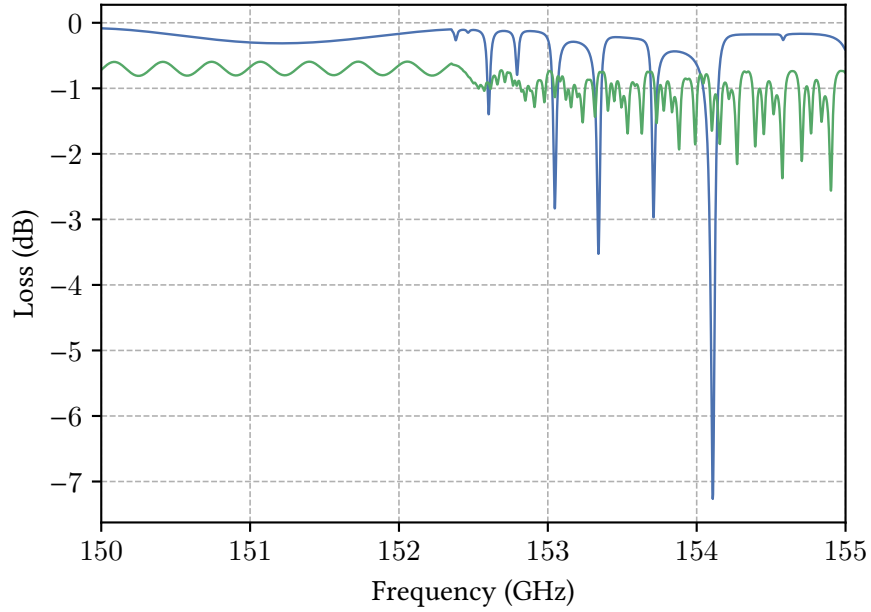
Figure 5.5: Transmission through a waveguide section with $l_2 = 5$ cm (blue line) and $l_2 = 40$ cm (green line) with a transition section that has been reduced from $l_{12} = 5$ mm to $l_{12} = 1$ mm compared to Figure 5.4.

tion section. Figure 5.5 shows that a reduction of the transition section length to $l_{12} = 1$ mm leads to much larger resonances due to the increased mode conversion. It is therefore desired to avoid short sections of waveguides placed in-between waveguides with smaller diameter and that any transition sections be as long as possible. There are some methods for reducing mode conversion by using complex transition profiles [57]. In the final design of the waveguide system those were not used, as linear transition sections could be designed long enough to reduce mode conversion sufficiently.

5.4. Free space transitions

There are two different vacuum stages inside the experimental setup, compare Figure 5.1. First, the microwaves need to be transmitted through a standard CF flange viewport to the prevacuum stage and then through a fused silica window leading to the trap chamber. Both transitions demand short gaps between waveguides. The mode matching method can not deal with free space regions, as the microwaves do not propagate in waveguide modes, limiting the estimations to FEM calculations with COMSOL.

Horn antennas are used to efficiently transmit microwaves into free space. The cross-section of the waveguide is increased in order to *match the impedance of the vacuum* [58], compare Eq. (4.7) with $k_z \to k$. For a conical horn there is a formula for the optimal horn aperture radius

r_horn given the slant length L of the conus and the wavelength λ of the microwaves:

$$r_\text{horn} = \sqrt{3\lambda L},\qquad\qquad(5.3)$$

which results in minimal reflections at the boundary to the free space region [59].

Antenna theory provides gain values for the far field of the microwaves radiated by the horn. However, for the purpose of this experiment, the free space regions are of the order of just a few wavelengths, making a far field approximation unsuitable. Additionally, the oversized waveguides with a radius of 4 mm used in this setup have a wave impedance of $Z \approx 0.99 Z_0$, which is already much closer to the impedance of the vacuum compared to the wave impedance of $Z \approx 0.68 Z_0$ of the single-mode waveguide with a radius of 800 µm. Therefore, the free space transitions relevant at this experiment can not be directly compared to standard use cases for horn antennas, making numerical calculations and measurements necessary in order to fix a final design for the experiment.

5.4.1. Transition to the prevacuum

First, the transition to the prevacuum is modelled. Starting from the microwave generator, WR6 waveguides connect to a pyramidal horn optimised, similar to Eq. (5.3), for the center of the WR6 band at 140 GHz [60]. The microwaves pass through the CF window and are picked up by a horn flanged to the 4 mm stainless steel oversized waveguide. The FEM calculations will concentrate on the transition from horn to horn and ignore the CF window for now. In order to reduce the geometry to two dimension, the WR6 waveguide is replaced by a cylindrical waveguide with radius $r_1 = 800$ µm and the WR6 horn by an equivalent optimal conical horn at 140 GHz, compare Eq. (5.3).

Figure 5.6 schematically shows the geometry used for the FEM calculation. For varying gap length l_gap and opening radius $r_\text{horn,2}$ the transmission of the TE_{11} mode is averaged over the interval from 148 to 166 GHz, see Figure 5.7. For the given length $l_\text{horn,2} = 3$ cm condi-
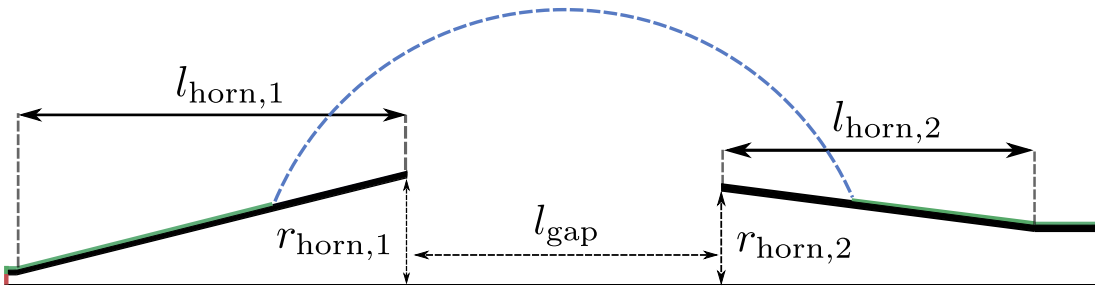

Figure 5.6: Schematic of the radial profile for the free space transitions calculated with COMSOL. The colours indicate boundary conditions: red for port, green for impedance and blue for scattering boundary condition. The solid black lines indicate material different from air, i.e. copper on the left and stainless steel on the right. The length $l_\text{horn,1} = 3.5$ cm, radius $r_\text{horn,1} = 8$ mm and length $l_\text{horn,2} = 3$ cm are fixed and $r_\text{horn,2}$ is varied.
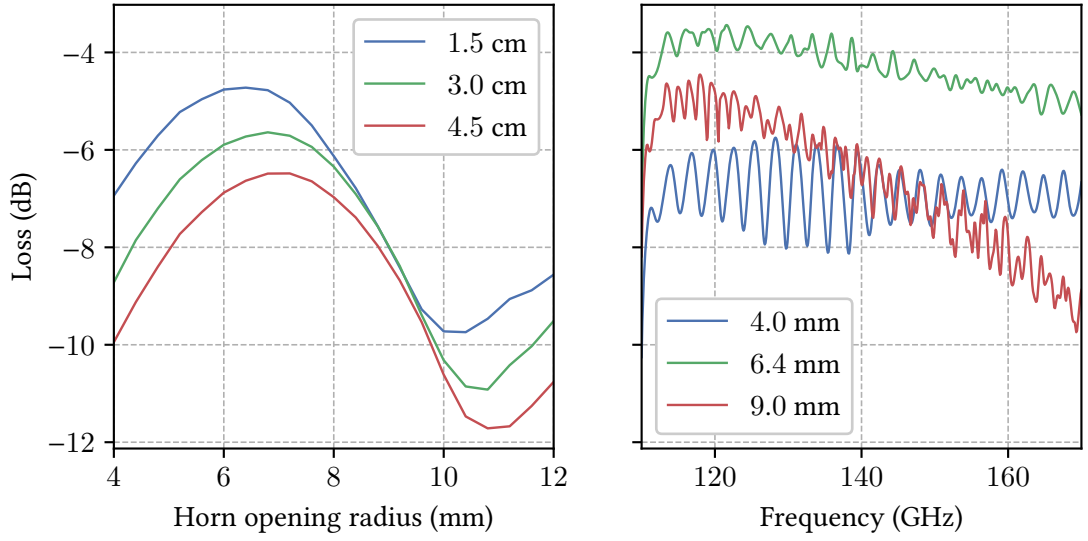
Figure 5.7: Left: For three different gap lengths l_{gap} the horn opening radius is varied and the mean transmission from 148 to 166 GHz is plotted. **Right:** Transmission for different horn opening radii and $l_{\mathrm{gap}} = 1.5$ cm.

tion Eq. (5.3) gives an optimal horn radius of $r_{\mathrm{horn},2} = 9$ mm. The FEM calculation, however, shows an optimal value between 6 and 7 mm which increases with l_{gap}. The transmission over the whole WR6 band with $r_{\mathrm{horn},2} = 9$ mm, the optimum value of $r_{\mathrm{horn},2} = 6.4$ mm and for an open ended waveguide, $r_{\mathrm{horn},2} = 4$ mm, is shown in Figure 5.7. Interestingly, the transmission spectrum with the open ended option has a clear sinusoidal shape that does not decrease with frequency as the other two options. Potentially, the open ended waveguide has the advantage of reducing trapped mode resonances, because modes forming on the first horn that do not *fit* into the oversized waveguide are just lost into free space.

In a cavity resonances build when an integer number of half wavelengths is equal to the cavity length L. These resonances are spaced by $\frac{c}{2L}$. By doing a Fourier transform of the transmission spectrum, trapped modes can be identified by the corresponding cavity length L, which appears as an extremum at the position $\frac{2L}{c}$. These length do not directly correspond to geometrical lengths, as the effective axial wavelength $\lambda_z = 2\pi/k_z$ varies with the radius of the waveguide. Nevertheless, increases in the gap size transform one to one to increases in the cavity length, because inside the gap the axial wavelength λ_z is equal to the free space wavelength λ, see Figure 5.8. This method is used in the measurements to identify trapped modes.

5.4.2. Transition to the trap chamber

Storing single charged ions over periods of several months, as is required for the ${}^3\mathrm{He}^+$ hyperfine structure measurements and for other g-factor measurements, requires a very good vacuum
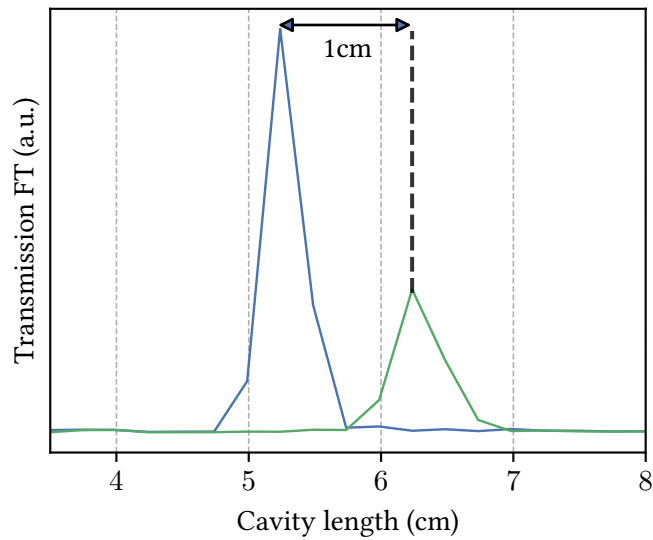
Figure 5.8: Part of the Fourier transform (absolute square) of the calculated transmission for $r_{\text{horn},2} = 4$ mm, $l_{\text{gap}} = 1.5$ cm (blue) and $l_{\text{gap}} = 2.5$ cm (green). The resolution is limited by the span of the frequencies for which the transmission is calculated. Here the WR6 frequencies from 110 to 170 GHz were used.

inside the trap chamber. To ensure this, the trap chamber is pumped separately and sealed off [5].

Figure 5.9 shows the transmission line connecting the 4 mm steel pipe with the trap tower. The waveguide is flanged to a long transition section reducing the radius to 2.5 mm in order to match the inner radius of the following copper tube[1]. At this section there should be essen-
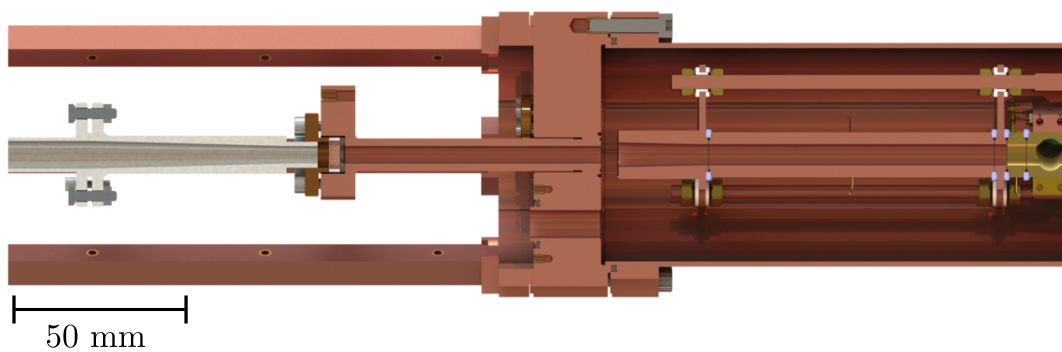

Figure 5.9: CAD render of the waveguide section leading to the trap chamber. For details see text.

---

[1]This part was originally designed to allow for a laser to be coupled into the trap and could not be redesigned for the microwave injection as it was already in the manufacturing process.
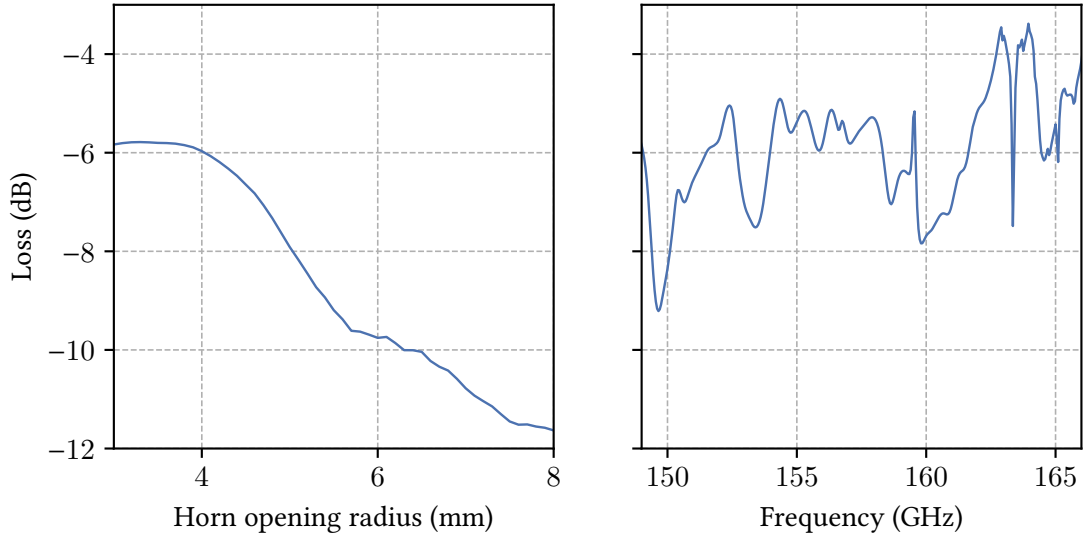
Figure 5.10: Left: For different horn opening radii, the mean transmission from 149 to 166 GHz is plotted. **Right:** Transmission for r_{horn} = 3.5 mm. The sharp drops in the transmission on the right were checked to be fully resolved by increasing the frequency resolution.

tially no reflections, as the preceding uniform section of waveguide is over 1 m long and any unwanted modes are sufficiently damped. To ensure that the different thermal properties of steel and copper do not lead to mechanical stress, the reduction piece is just tucked into the next piece of pipe, leaving some room for thermal expansion. A fused silica window, which is cryogenically sealed with indium, is used as a viewport for the microwaves. In order to mechanically decouple the trap tower, it can not be connected directly to the trap chamber flange. A copper horn with a small opening angle connects to a long electrode with a radius of 3 mm.

The reducing piece could be chosen sufficiently long to avoid any mode conversion. To reduce the number of trapped modes, the diameter of the glass window was chosen just large enough (5 mm) such that there is still enough contact surface to seal the vacuum. That leaves the horn opening radius as the only parameter to be optimised. Using COMSOL, the transmission through the geometry of Figure 5.9, starting from the end of the reducing piece and ending just after the horn connected to the trap tower, is calculated. The glass window was included in the COMSOL calculation by introducing a region with a relative permittivity of ϵ_r = 2.4 at its position.

The average transmission over the relevant frequencies from 148 to 166 GHz was used to find the optimal horn opening radius, see Figure 5.9. The open ended waveguide option produces a good result with the optimal radius of $r_{\text{opt}} \approx 3.5$ mm being just slightly better. Nevertheless, a horn with an opening radius of 3.5 mm is still used in the final geometry. This should allow for slight misalignments of the trap tower relative to the flange, as more solid angle is covered compared to the open ended option. Comparing with the ideal horn equation (5.3), which gives $r_{\text{opt}} \approx 7.4$ mm, this shows once more that the standard arguments are not valid here.
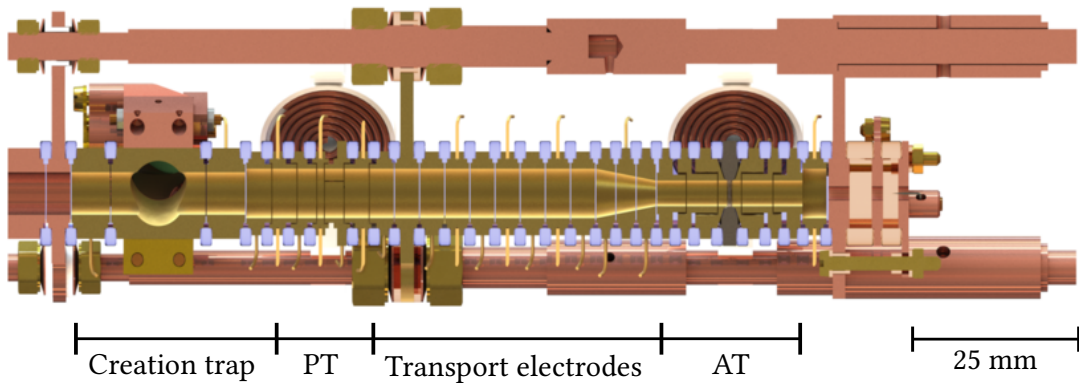
| Creation trap | PT | Transport electrodes | AT | 25 mm |

Figure 5.11: CAD render of the trap tower used for the hyperfine structure measurement. The radii are $r_{CT} = 3$ mm for the creation trap, $r_{PT} = 3.5$ mm for the precision trap and the transport electrodes and $r_{AT} = 1.8$ mm for the analysis trap. The trap electrodes are all gold plated.

5.5. Microwave field inside the Penning traps

Due to the non-uniformity of the section preceding the precision trap and the linear transition section leading to the analysis trap, the microwave field is not a that of a single forward propagating TE_{11} mode. The interference of modes causes local minima in the transverse field amplitude, which may even be at the ion's exact position. Especially in the analysis trap, where the highest microwave power is needed, this may lead to insufficient spin-flip rates.

Figure 5.11 shows the trap tower. The small gaps introduced by the sapphire spacers are approximately 100 μm thick and can be neglected as this is much less than the wavelength of the microwaves. In contrast, the hole with a radius of 8 mm through which atoms enter the creation trap is larger than a wavelength and is expected to have some influence. As the hole destroys the cylindrical symmetry, it is not included in the calculations and an estimate is made later. There is a linear transition section reducing the radius from the precision trap to the analysis trap. At this section microwaves are reflected, including power of the fundamental TE_{11} mode. This may lead to additional interference in the precision trap. It will be assumed that no reflection happens after the analysis trap. Experimentally this is realised by inserting a microwave absorbing cone made of a carbon nanotube peek material [61] into the last trap electrode, compare [32]. Apart from the TE_{11}, the TM_{11} and TE_{12} mode propagate in the forward direction inside the analysis trap.

Because it can not be assumed that a single mode enters the precision trap, the geometry of Figure 5.9 has to be included in the calculation. The absolute value of the radial magnetic field on the axis of the analysis trap is calculated with COMSOL. This is done in a 0.5 GHz interval around the two frequencies of 157.5 and 148.8 GHz such that any frequency dependence may become clear. In order to compare these values with the loss values calculated before, they are transformed into effective power loss values of the TE_{11} mode using Eq. (5.1) and the corresponding radius of $r_{AT} = 1.8$ mm.
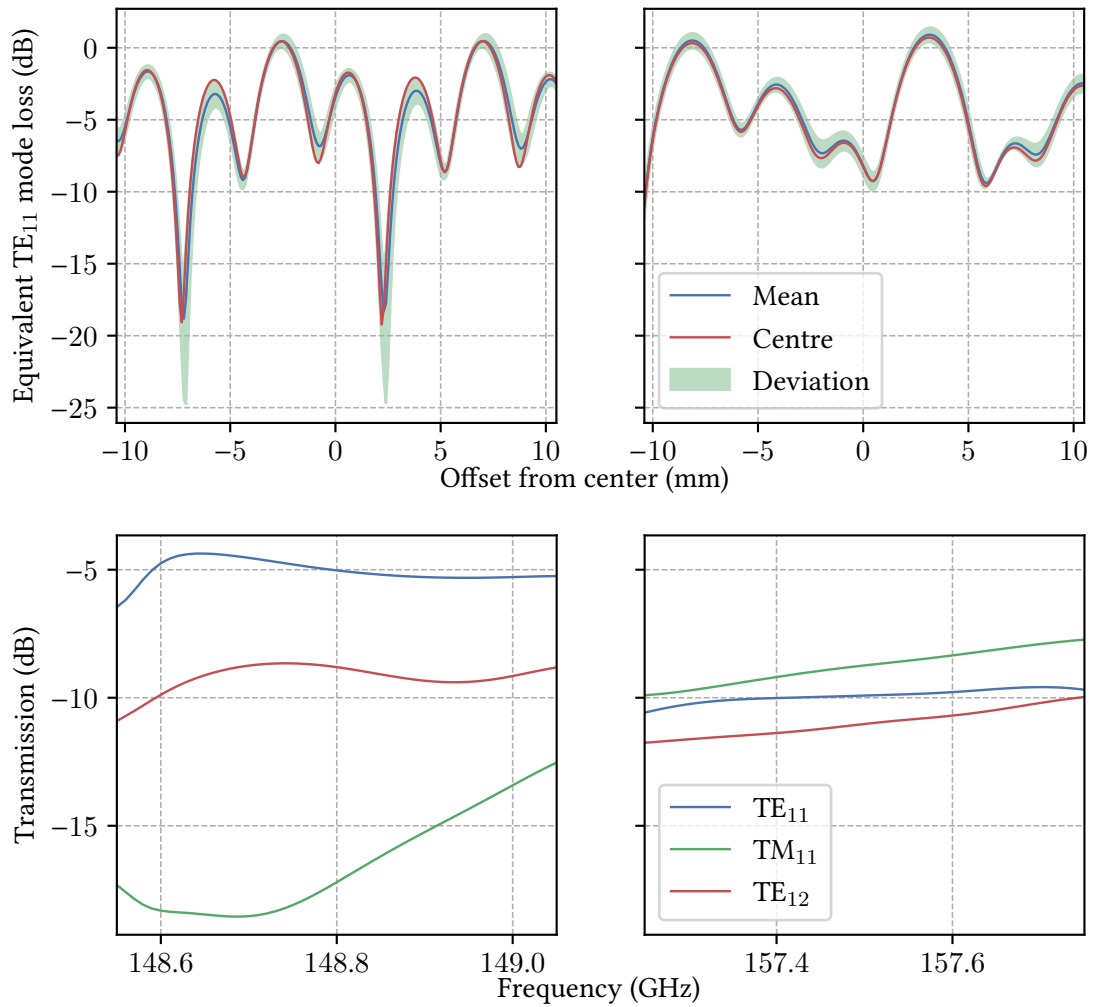
Figure 5.12: Top: Equivalent TE_{11} mode power calculated from the radial magnetic field on axis in the analysis trap for the two transition at 148.8 (left) and 157.5 GHz (right). The blue curves are the mean transition over a 0.5 GHz interval, the green areas are standard deviations of transmission in that frequency interval and the red curves are the values at the center frequencies. **Bottom:** Transmission of modes into the analysis trap, given only a TE_{11} mode at the input. These curves corresponds to values according to Eq. (4.16) with $n = TE_{11}$ and $m = TE_{11}, TM_{11}, TE_{12}$.

Figure 5.12 shows the result of the calculation. From the lower graphs it becomes clear that there is considerable power converted to the TM_{11} and TE_{12} modes leading to the interference patterns of the upper magnetic field plots. For the lower frequency the two destructive interference minima are well away from the center of the trap. The effective losses at the center of the analysis trap, starting from the quartz glass window at the trap chamber flange, can be estimated to be no worse than -10 dB.

5.6. Overview and total loss

While designing the microwave transmission line it is crucial to avoid any non-uniformities of the waveguide wherever possible. This reduces mode conversion and the possibility of trapped modes. The optimisation of the microwave horns with the finite element method showed that the horn opening radii calculated with the ideal horn equation (5.3) do not yield optimal transmission for short gaps and oversized waveguides and that an individual optimisation is necessary.

The waveguide microwave injection can be split up into individual parts characterised by the corresponding power loss of the fundamental TE_{11} mode. In the following the individual sections are summarised:

Source to first horn: A single mode propagates through standard straight WR6 waveguide pieces to the first microwave horn. In order to reduce the magnetic field the microwave generator experiences, 0.3 m of waveguide are placed between it and the horn. This results in a loss of about -3 dB [47].

Transition to prevacuum: The standard WR6 gain horn transmits microwaves through a CF window. A waveguide with a radius of 4 mm picks up the microwaves after a gap length less than 4.5 cm. The use of a horn on this side of the waveguide was omitted to reduce trapped modes, see also the measurements in Figure 6.3. A FEM calculation of the losses was done using an idealised cylindrical geometry that does not include the window, see Figure 5.6. This will later be expanded on in the measurements. The expected losses from the calculation are of the order of -10 dB, see Figure 5.7. Displacements of the standard gain horn relative to the oversized waveguide are estimated in Appendix B.2 and show no large additional losses.

Long oversized waveguide section: A long stainless steel pipe with a radius of 4 mm transmits the microwaves over a length of 1.5 m, see Figure 5.1. A reducing piece with a length of 5.7 cm connects to a smaller section with a radius of 2.5 mm. The transmission over this large section can be efficiently calculated with the mode matching technique and is found to be no less than -3 dB with nearly no frequency dependence. This is consistent with the ohmic loss of a 1.5 m long stainless steel pipe with 4 mm radius, compare Eq. (4.13).

Transition to the trap chamber and to the analysis trap: A fused silica window followed by a copper pipe couples the microwaves into the trap chamber. A small horn with a radius of 3.5 mm picks up the microwaves and a following electrode connects to the Penning traps, see Figure 5.9 and 5.11. The field on the axis of the analysis trap is calculated with the finite element method resulting in effective losses with a lower bound of -10 dB at the ion's position. The hole in the creation trap can be modelled as a gap of 8 mm between two waveguides of 3 mm radius. A FEM calculation of this model results in losses bounded by -2.5 dB, see Figure B.1.

The total calculated losses sum up to about -29 dB and are two orders of magnitude above the maximum of -53 dB of allowed losses. It is expected that additional sources of power loss

will be present in the experimental setup, for example losses due to imperfections of the parts constructed in the workshop or oxidation of copper surfaces. In the next chapter some of the sections presented here are analysed with measurements and the total losses are updated.

6. Waveguide measurements

In the last chapter, the usage of oversized waveguides for the transmission of the high-frequency microwaves at about 150 GHz was motivated and investigated with finite element and mode matching methods. For the final optimised waveguide geometry an estimate using these techniques for the total expected losses was calculated, compare Section 5.6. These results are now compared to explicit measurement of the microwave transmission through oversized waveguides and part of the assembled waveguide transmission line.

6.1. Measurement procedure

Measurement of the power transmitted through waveguide components is done with a WR6 amplitude diode detector from Sage Millimeter [62]. The detector is provided with a calibration of the frequency dependant measured voltages per input power. Similarly, the signal generator extension (SGX) module from VDI [49] came with a calibration of the saturated output power at a given frequency. As those calibrations where provided only in steps of 2 GHz and 0.6 GHz over the D-Band of $110-170$ GHz for the detector and SGX, respectively, they were interpolated to the desired frequency resolution.

The VDI SGX module multiplies an input microwave signal, provided here by an Anritsu MG3692C signal generator, by a factor of 12. Internally the SGX module has two passive multiplier stages with multiplication factors of 3 and 4 and active amplification after each stage. The output power of the SGX module saturates for input powers higher than 5 dBm. It is not possible to consistently use the SGX module below the saturation power, as the output power does not scale linearly with the input power. By sweeping the frequency of the Anritsu signal generator from 9.16 GHz to 14.17 GHz and measuring the voltage on the detector, a transmission spectrum over the WR6 frequencies is generated.

To check the calibration of the detector and the saturated output power of the SGX module, the power transmitted through a single two inch long WR6 waveguide is measured, see Figure 6.1. The waveguide should only account for around 1 dB of losses. Thus, there is a big discrepancy between the measured power and the saturated power provided by the manufacturer. A possible explanation is a power dependence of the detector's sensitivity. The sensitivity is defined as the slope of the measured voltage U given an input microwave power $P(\nu)$ at a frequency ν, i.e. Sensitivity $= \frac{d}{dP(\nu)}U|_{P(\nu)}$. As the sensitivity is only provided at
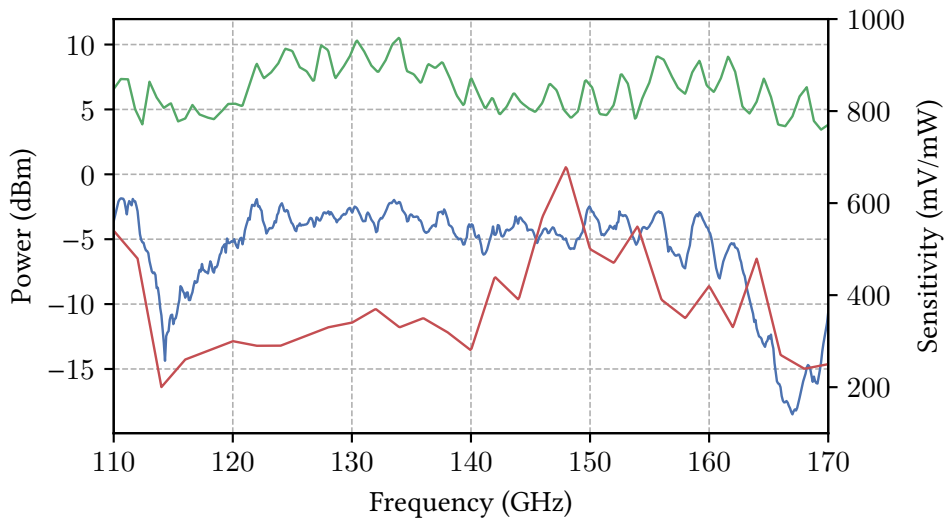
Figure 6.1: The measured power transmitted through a single two inch long WR6 waveguide is shown in blue. To transform the measured voltages to power the calibration of the detector was used. The saturated power of the microwave frequency multiplier provided by the manufacturer is shown in green. The sensitivity of the detector at -20 dBm input microwave power is shown in red.

-20 dBm, see Figure 6.1, it might be very different at the saturation power of the SGX module. There is only limited information available on the acquired detector, but as the diode is zero biased it is most likely a Schottky diode detector comparable to [63]. These kinds of detectors have a linear voltage to power response only in a square-law region of input power and different response at higher powers. Additionally, the measured power shows large losses at the edges of the D-band, which seem to be correlated with the detector sensitivity, even though it is already included in the conversion from measured voltage to power. This indicates that the discrepancy is rather a problem of the detector performance than the SGX module. Nevertheless, because there is no other means to measure the saturated output power of the SGX module, it can not be ruled out that it is largely below its specifications.

For the measurements, the circular waveguide section, referred to as the device under testing (DUT), is placed in-between two WR6 standard gain horns, which are connected to the SGX module and detector, respectively, see Figure 6.2. This enables an easy way to exchange two DUTs and test them against each other. The transition between horn and DUT will be explained in more detail for the individual measurements. All measurements will be shown as the loss relative to the absolute measurement of Figure 6.1, referred to as the calibration measurement. Essentially only the S_{21} parameter of the transmitted fundamental TE_{01} rectangular waveguide mode can be measured with this setup.
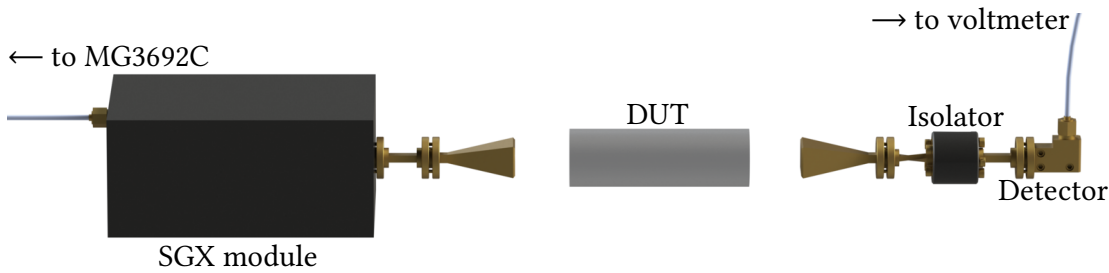
Figure 6.2: Experimental setup for the waveguide transmission measurements. The circular piece of waveguide (i.e. the DUT) is placed in-between two WR6 pyramidal standard gain horns connected to the SGX module and the detector, respectively. A faraday isolator is placed before the detector in order to dampen reflected waves by 30 dB.

6.2. Horn-horn transitions

In Section 5.4.1, the transition from the standard gain horn to a horn connected to an oversized circular waveguide section was investigated with COMSOL using an idealised symmetrical geometry. Now a circular piece of waveguide of 49.5 cm[1] length and radius of 4 mm with and without conical horns flanged to each end is placed in-between the two rectangular horns as the DUT, compare Figure 6.2. The horns were designed with respect to the optimal horn equation, Eq. (5.3), with a length of 3 cm and opening radius of 9 mm and manufactured at the MPIK workshop.

Figure 6.3 shows the measured loss through the setup. The loss graphs reveal much more severe resonances for the options with the conical horns than without them. These large resonances are spaced by a few GHz, which corresponds to cavity lengths of a few centimetres. Only the transitions from the pyramidal horn to the conical horn form a cavity like structure of that size. Similar to the discussion in Section 5.4.1, it is expected that without the conical horns the trapped mode resonances disappear, because the field structures are not reflected at the oversized section but just lost into free space. That the resonances are much deeper than seen in the calculations of Figure 5.7 may be connected to the idealised symmetrical geometry of the FEM calculation. In conclusion, this shows that the option without horns on the oversized section is safer in terms of trapped mode resonances. Keeping in mind that here two free space transitions occur, the measured absolute transmission values are no worse than expected from the calculation.

Again, the loss graphs show smaller transmission at the edges of the D-band, which seem to be correlated to the detector calibration shown in Figure 6.1, even though the calibration measurement is subtracted. This once more indicates some non-linearity of the detectors response.

---

[1]It was cut to be 50 cm but one end needed to be reworked as it became slightly oval.
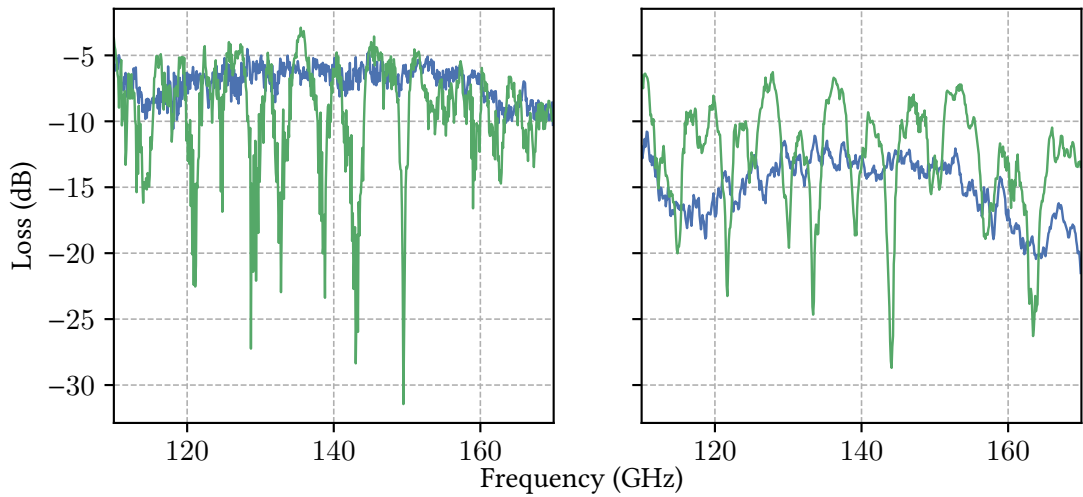
Figure 6.3: Measurement of the transmission through the oversized waveguides with (green) and without (blue) conical horns. On the left the free space distance is 0 cm and on the right it is 4 cm.

6.3. Damping of resonances

To investigate the damping of trapped mode resonances, two $r = 4$ mm oversized waveguides with lengths of 49.5 cm and 100 cm, respectively, are used as the DUT, compare Figure 6.2. The distance between the horns and the oversized waveguide is chosen to be 0 cm. Modes are effectively trapped only between the two pyramidal horns, as there should be no reflection between the pyramidal horn and the oversized waveguide directly.

Figure 6.4 shows the results of the transmission measurement. From the upper graph it is already visible, that the longer waveguide section produces faster repeating resonances. The amplitude of these resonances decreases for the longer section. Using the Fourier transformation, see the lower plot of Figure 6.4, to find corresponding cavity lengths as described in Section 5.4.1 clearly indicates that the modes are trapped between the two pyramidal horns. The decrease in amplitude of the resonances is also visible.

The increase of cavity length by ~ 51.5 cm for the largest peaks and by ~ 52.5 cm for the second largest indicates that the modes reflected have small mode numbers. For the TE_{11} mode inside a 4 mm waveguide the axial wavelength is $\lambda_z/\lambda \approx 1.011$ at 140 GHz, compare Eq. (4.11). Scaling the increase of 50.5 cm of the waveguide with this ratio gives a length of 51.13 cm. Similarly, for the TM_{11} mode, this gives a value of 53.43 cm and for the TE_{12} mode a value of 56.69 cm. From this it can be concluded that the rectangular TE_{01} waveguide mode originating from the WR6 waveguide is mainly converted to the circular waveguide TE_{11} mode.
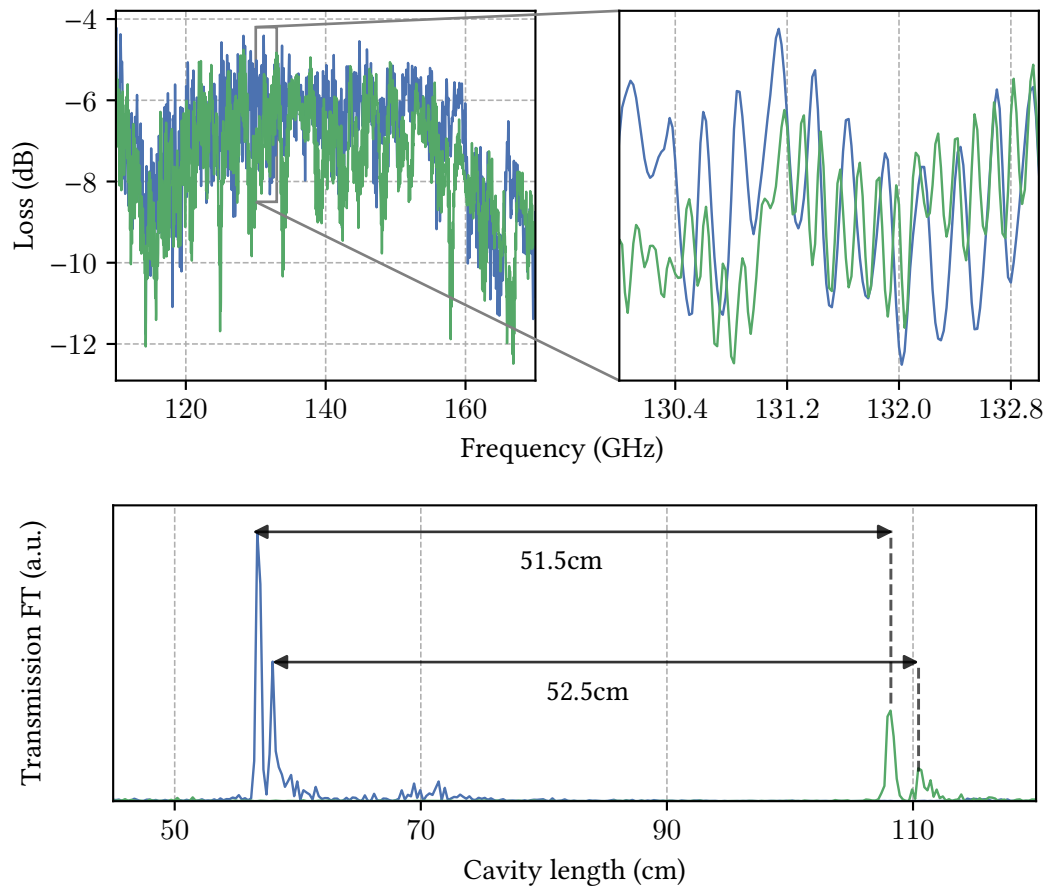
46

Figure 6.4: Top: Loss through $r = 4$ mm oversized waveguides with lengths of 49.5 cm (blue) and 100 cm (green), respectively. **Bottom:** Absolute value of the Fourier transform of the loss spectrum from the top graph as a function of effective cavity length. The resolution of the Fourier transform is limited by the WR6 band span and evaluates to 0.25 cm.

6.4. Transmission through the completed oversized stainless steel section

As the assembly of the experiment progressed, it was possible to measure the microwave transmission through the finished oversized stainless steel waveguide sections, compare Figure 6.5. For this measurement the total length of WR6 waveguide leading to the standard gain horn is 30 cm and the distance from the horn to the glass window is 0.5 cm. The total distance from the horn to the oversized waveguide is 4 cm. A horizontal alignment of the horn above the glass window is realised with the setup shown on the right side of Figure 6.5. An optimisation of the alignment is done by sight and by maximising the detector signal at a specific frequency.
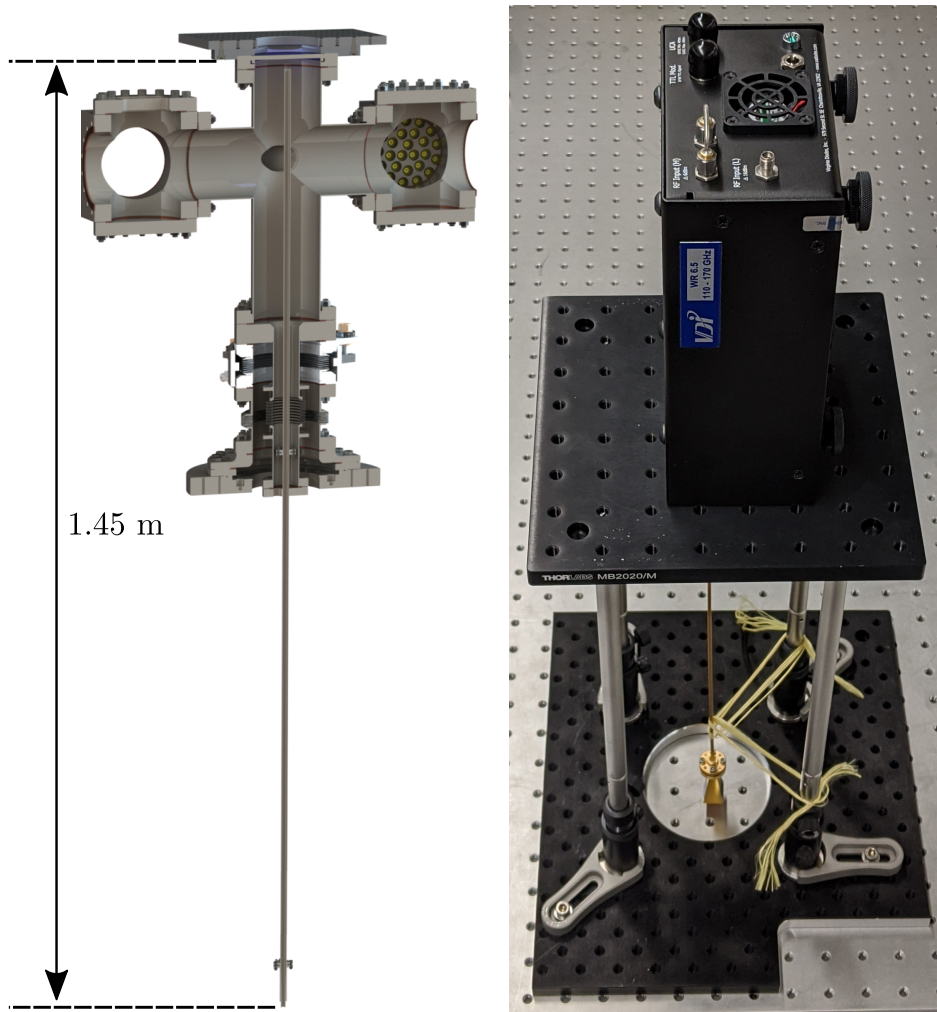
Figure 6.5: Left: CAD render of the oversized stainless steel waveguide section used as the DUT. The window inside the top CF flange is 1 cm thick. **Right:** Picture of the mount for the SGX module above the top flange. The round cutout in the lower optic breadboard is centered with respect to the glass window in the top flange. As the long pieces of WR6 waveguide are not perfectly straight and the stainless steel tube inside the experiment is not ideally aligned with the center of the window a manual horizontal adjustment of the standard gain horn is necessary.

The standard gain horn connected to the detector is placed at a distance of around 1 cm to the reducing stainless steel piece.

Figure 6.6 shows the results of the measurement after two independent horizontal alignment procedures. There is only a slight difference between the two measurements, indicating that the alignment is not a big issue, compare also the estimate in Appendix B.2. At around 160 to 170 GHz the losses show a decrease that has a form similar to the increase of losses seen in the
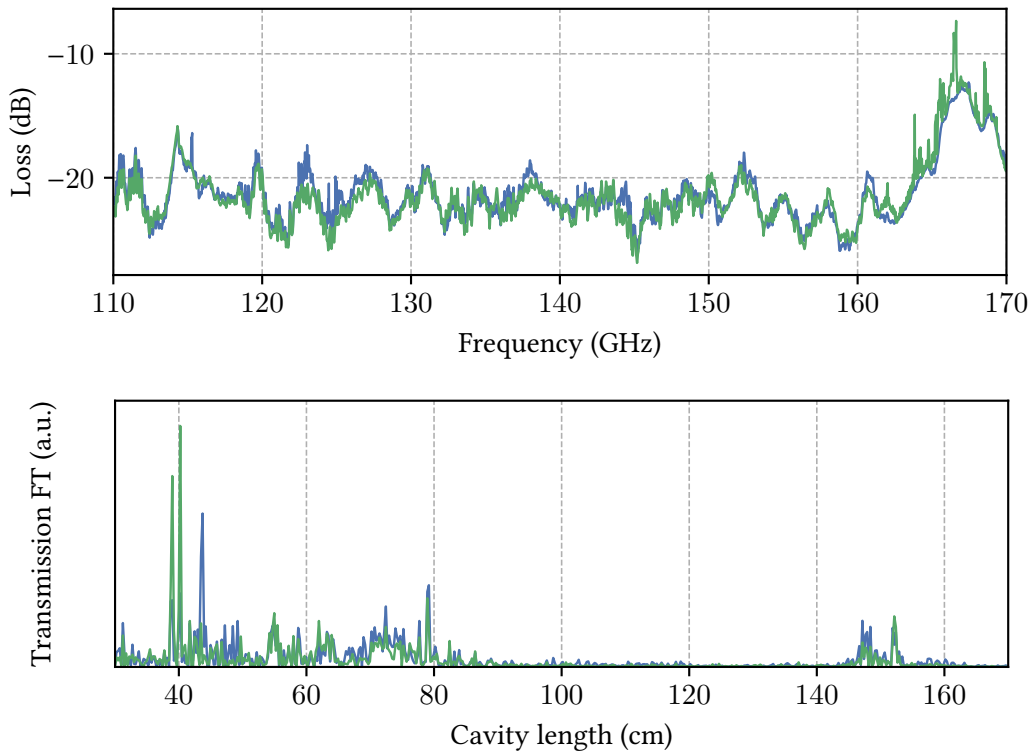
Figure 6.6: Top: Measurement of the transmission through the setup shown in Figure 6.5 for two independent alignment procedures. The measured signal is still well above the detectors smallest detectable signal at around -50 dBm. **Bottom:** Fourier transform of the above measurements.

calibration measurement of Figure 6.1 indicating a detector artefact. The fast oscillations on the measured signal from modes trapped between the two horns are comparably smaller than the ones measured in the previous section, compare Figure 6.4, again showing the damping of these resonances.

In the Fourier transform of the measurement, see Figure 6.6, the resonance between the two horns appear as comparably smaller peaks at around 150 cm corresponding to about the distance between the horns. There are several larger peaks between 30 and 90 cm which could be attributed to some reflections happening directly between one horn and a structure in the assembly that is not part of the transmission line.

The total transmitted power is mostly above -25 dB. In the estimates made in the overview of Section 5.6 which amount to -13 dB, the glass window and the second free space transition to the detector were not included. The loss due to the latter is estimated with a FEM calculation similar to the one in Section 5.4.1 resulting in losses of about -9 dB. It seems plausible that the additional losses of -3 dB compared to the estimate originate from the glass window in the CF flange.

7. Conclusion and outlook

At the *Max Planck Institute for Nuclear Physics*, a new Penning-trap experiment is set up to measure the hyperfine structure of $^3\text{He}^+$. With the intended measurement precision, the bound electron and nuclear g-factors will be determined with a relative uncertainty of 10^{-10} and 10^{-9}, respectively, and the zero-field hyperfine splitting of the ground state with an uncertainty better than 10^{-10}. In this work, the theoretical and experimental challenges of driving the hyperfine transitions of $^3\text{He}^+$ inside a Penning trap were investigated.

In a first step, the frequencies of the transitions of the hyperfine structure were derived. As no Penning-trap experiment has investigated a system with a hyperfine structure before, theoretical considerations were necessary to map the transitions of the four-level system to effective two-level systems which allowed the usage of the lineshape calculations of Brown and Gabrielse [19]. These lineshape calculations lead to the probability to drive a hyperfine transition given input microwaves detuned from the transition frequency. Driving the transitions with maximum probability on resonance gives relatively strict requirements on the microwave power in the analysis trap, where electron spin transitions are used for detecting spin-flips.

Because of the high power requirement and the high frequencies of the electron spin transitions at 150 GHz, waveguides need to be used to couple the microwaves into the Penning traps. Due to the restrictions imposed by the experimental setup and construction difficulties, standard waveguides are not practical to use inside the setup. By using oversized waveguides made of readily available stainless steel pipes, the heat load can be reduced drastically compared to standard copper waveguides without increasing the microwave losses in the uniform sections. To deal with the challenges arising at transitions sections, a numerical mode matching technique building on the theory describing the mode propagation inside waveguides is derived.

Using the mode matching technique and FEM calculations with COMSOL, the oversized waveguide leading to the Penning traps is optimised for maximum transmission given the restrictions imposed by the experimental setup. Special care had to be taken with trapped mode resonances forming in cavity like structures of the waveguide which cause large drops in the transmission. It was found that these resonances can be sufficiently damped for long enough oversized waveguide sections.

Lastly, detailed transmission measurements through oversized waveguide sections were performed, which confirmed the previous considerations. The total expected losses from the nu-

merical calculations and the measurement sum up to -32 dB, which is well above the maximum of allowed losses of -53 dB. Potentially, the microwave multiplier is not providing the power it is specified for, as the calibrations of the detector and the microwave multiplier provided by the manufacturers were not consistent with a calibration measurement. Nevertheless, even with the measured performance enough power would still arrive at the ion's position.

Current status of the experiment

As of the end of this thesis, the experiment has been fully assembled, see for example the assembled trap tower in Figure 7.1. The waveguide transmission line for the electron spin transitions is fully implemented in the setup. Further, for the nuclear transitions at about 4 GHz, semi-rigid coaxial cables with low heat conductivity and microwave losses of about -10 dB lead directly into the trap chamber. Inside the trap chamber, two coils next to the analysis and precision trap produce a radial magnetic field component at the center of the trap.

Loading of $^3\text{He}^+$ using the glass sphere as an atom source and a field emission point, described in [46], has been achieved inside a simplified Penning-trap apparatus. For both analysis and precision trap, axial detection systems have been build and tested. An additional cyclotron detection system for the precision trap has also been implemented. Following some further tests, the experiment will be inserted into the superconducting magnet system and Penning-trap measurements can start.

Figure 7.1: Photograph of the assembled trap tower.

Bibliography

1. Dehmelt, H. Continuous Stern-Gerlach effect: Principle and idealized apparatus. *Proceedings of the National Academy of Sciences of the United States of America* **83,** 2291–2294. doi:10.1073/pnas.83.8.2291 (1986).

2. Hanneke, D., Fogwell, S. & Gabrielse, G. New Measurement of the Electron Magnetic Moment and the Fine Structure Constant. *Phys. Rev. Lett.* **100,** 120801. doi:10.1103/PhysRevLett.100.120801 (2008).

3. Sturm, S. *et al. g* Factor of Hydrogenlike $^{28}\mathrm{Si}^{13+}$. *Phys. Rev. Lett.* **107,** 023002. doi:10.1103/PhysRevLett.107.023002 (2011).

4. Van Dyck, R. S., Schwinberg, P. B. & Dehmelt, H. G. New High-Precision Comparison of Electron and Positron *g* Factors. *Phys. Rev. Lett.* **59,** 26–29. doi:10.1103/PhysRevLett.59.26 (1987).

5. Mooser, A. *et al.* Direct high-precision measurement of the magnetic moment of the proton. *Nature* **509,** 596–599. doi:10.1038/nature13388 (2014).

6. Schneider, G. *et al.* Double-trap measurement of the proton magnetic moment at 0.3 parts per billion precision. *Science* **358,** 1081–1084. doi:10.1126/science.aan0207 (2017).

7. Smorra, C. *et al.* A parts-per-billion measurement of the antiproton magnetic moment. *Nature* **550,** 371–374. doi:10.1038/nature24048 (2017).

8. Sturm, S., Werth, G. & Blaum, K. Electron *g*-factor determinations in Penning traps. *Annalen der Physik* **525,** 620–635. doi:10.1002/andp.201300052 (2013).

9. Bluhm, R., Kostelecký, V. A. & Russell, N. CPT and Lorentz tests in Penning traps. *Physical Review D* **57,** 3932–3943. doi:10.1103/physrevd.57.3932 (1998).

10. Schuessler, H. A., Fortson, E. N. & Dehmelt, H. G. Hyperfine Structure of the Ground State of $^{3}\mathrm{He}^{+}$ by the Ion-Storage Exchange-Collision Technique. *Phys. Rev.* **187,** 5–38. doi:10.1103/PhysRev.187.5 (1969).

11. Fermi, E. Über die magnetischen Momente der Atomkerne. *Zeitschrift für Physik* **60,** 320–333. doi:10.1007/BF01339933 (1930).

12. Karshenboim, S. G. & Ivanov, V. G. Hyperfine structure of the ground and first excited states in light hydrogen-like atoms and high-precision tests of QED. *The European Physical Journal D - Atomic, Molecular, Optical and Plasma Physics* **19,** 13–23. doi:10.1140/epjd/e20020050 (2002).

13. Fei, X., Hughes, V. & Prigl, R. Precision measurement of the magnetic field in terms of the free-proton NMR frequency. *Nuclear Instruments and Methods in Physics Research Section A: Accelerators, Spectrometers, Detectors and Associated Equipment* **394,** 349–356. doi:10.1016/S0168-9002(97)84161-7 (1997).

14. Nikiel, A. *et al.* Ultrasensitive ^{3}He magnetometer for measurements of high magnetic fields. *Eur. Phys. J. D* **68,** 330. doi:10.1140/epjd/e2014-50401-3 (2014).

15. Rudziński, A., Puchalski, M. & Pachucki, K. Relativistic, QED, and nuclear mass effects in the magnetic shielding of ^{3}He. *The Journal of Chemical Physics* **130,** 244102. doi:10.1063/1.3159674 (2009).

16. Flowers, J. L., Petley, B. W. & Richards, M. G. A Measurement of the Nuclear Magnetic Moment of the Helium-3 Atom in Terms of that of the Proton. *Metrologia* **30.** doi:10.1088/0026-1394/30/2/004 (1993).

17. Bennett, G. W. *et al.* Measurement of the Negative Muon Anomalous Magnetic Moment to 0.7 ppm. *Phys. Rev. Lett.* **92,** 161802. doi:10.1103/PhysRevLett.92.161802 (2004).

18. Otani, M. *Status of the Muon g-2/EDM Experiment at J-PARC (E34)* in *Proceedings of the 2nd International Symposium on Science at J-PARC — Unlocking the Mysteries of Life, Matter and the Universe* (2015). doi:10.7566/JPSCP.8.025008.

19. Brown, L. S. & Gabrielse, G. Precision spectroscopy of a charged particle in an imperfect Penning trap. *Phys. Rev. A* **25,** 2423–2425. doi:10.1103/PhysRevA.25.2423 (1982).

20. Ulmer, S. *First Observation of Spin Flips with a single Proton stored in a cryogenic Penning trap* PhD thesis (Ruperto-Carola University of Heidelberg, 2011). doi:10.11588/heidok.00012306.

21. Gabrielse, G., Haarsma, L. & Rolston, S. Open-endcap Penning traps for high precision experiments. *International Journal of Mass Spectrometry and Ion Processes* **88,** 319–332. doi:10.1016/0168-1176(89)85027-X (1989).

22. Ketter, J., Eronen, T., Höcker, M., Streubel, S. & Blaum, K. First-order perturbative calculation of the frequency-shifts caused by static cylindrically-symmetric electric and magnetic imperfections of a Penning trap. *International Journal of Mass Spectrometry* **358,** 1–16. doi:10.1016/j.ijms.2013.10.005 (2014).

23. Wineland, D. J. & Dehmelt, H. G. Principles of the stored ion calorimeter. *Journal of Applied Physics* **46,** 919–930. doi:10.1063/1.321602 (1975).

24. Ulmer, S. *et al.* Direct Measurement of the Free Cyclotron Frequency of a Single Particle in a Penning Trap. *Phys. Rev. Lett.* **107,** 103002. doi:10.1103/PhysRevLett.107.103002 (2011).

25. Cornell, E. A., Weisskoff, R. M., Boyce, K. R. & Pritchard, D. E. Mode coupling in a Penning trap: π pulses and a classical avoided crossing. *Phys. Rev. A* **41,** 312–315. doi:10.1103/PhysRevA.41.312 (1990).

26. Sturm, S., Wagner, A., Schabinger, B. & Blaum, K. Phase-Sensitive Cyclotron Frequency Measurements at Ultralow Energies. *Phys. Rev. Lett.* **107,** 143003. doi:10.1103/PhysRevLett.107.143003 (2011).

27. Brown, L. S. Geonium lineshape. *Annals of Physics* **159,** 62–98. doi:10.1016/0003-4916(85)90192-7 (1985).

28. Brown, L. S. & Gabrielse, G. Geonium theory: Physics of a single electron or ion in a Penning trap. *Rev. Mod. Phys.* **58,** 233–311. doi:10.1103/RevModPhys.58.233 (1986).

29. Feynman, R., Leighton, R. & Sands, M. *The Feynman Lectures on Physics, Vol. III: The New Millennium Edition: Quantum Mechanics* ISBN: 978-0-465-02501-5 (Basic Books, 2011).

30. Frasca, M. A modern review of the two-level approximation. *Annals of Physics* **306,** 193–208. doi:10.1016/S0003-4916(03)00078-2 (2003).

31. Schneider, G. *300 ppt Measurement of the Proton g-Factor* https://publications.UB.Uni-Mainz.DE/theses/frontdoor.php?source_opus=100002039&la=de. PhD thesis (Johannes Gutenberg-Universität Mainz, 2018).

32. Sturm, S. *et al.* The ALPHATRAP experiment. *Eur. Phys. J. Special Topics* **227,** 1425–1491. doi:10.1140/epjst/e2018-800225-2 (2019).

33. COMSOL AB, Stockholm, Schweden. *COMSOL Multiphysics v. 5.4.*

34. Häffner, H. *et al.* Double Penning trap technique for precise g factor determinations in highly charged ions. *The European Physical Journal D - Atomic, Molecular, Optical and Plasma Physics* **22,** 163–182. doi:10.1140/epjd/e2003-00012-2 (2003).

35. Mooser, A. *et al.* A New Experiment for the Measurement of the *g*-Factors of ^{3}He$^+$ and ^{3}He^{2+}. *Journal of Physics: Conference Series* **1138,** 012004. doi:10.1088/1742-6596/1138/1/012004 (2018).

36. Bloch, F. Nuclear Induction. *Phys. Rev.* **70,** 460–474. doi:10.1103/PhysRev.70.460 (1946).

37. Sturm, S. *et al.* High-precision measurement of the atomic mass of the electron. *Nature* **506,** 467–470 (2014).

38. Heiße, F. *et al.* High-Precision Measurement of the Proton's Atomic Mass. *Phys. Rev. Lett.* **119,** 033001. doi:10.1103/PhysRevLett.119.033001 (2017).

39. Zafonte, S. L. & Dyck, R. S. V. Ultra-precise single-ion atomic mass measurements on deuterium and helium-3. *Metrologia* **52.** doi:10.1088/0026-1394/52/2/280 (2015).

40. Maxwell, J. A dynamical theory of the electromagnetic field. *Phil. Trans. R. Soc* **155.** doi:10.1098/rstl.1865.0008 (1865).

41. Jackson, J. *Classical Electrodynamics, 3rd Edition* chap. 8. ISBN: 978-8-126-51094-8 (Wiley India Pvt. Limited, 2007).

42. Balanis, C. *Advanced Engineering Electromagnetics, 2nd Edition* 495–500. ISBN: 978-1-118-21348-3 (Wiley, 2012).

43. Omar, A. S. & Schonemann, K. Transmission Matrix Representation of Finline Discontinuities. *IEEE Transactions on Microwave Theory and Techniques* **33,** 765–770. doi:10.1109/TMTT.1985.1133124 (1985).

44. Chew, W. C. *Lectures on Theory of Microwave and Optical Waveguides* http://wcchew.ece.illinois.edu/chew/course/tgwAll20160215.pdf. (2016).

45. Guennebaud, G., Jacob, B., *et al. Eigen v3* http://eigen.tuxfamily.org.

46. Schneider, A. *Design of the Analysis Trap and He Ion Source for the $^3He^{2+}$ magnetic moment measurement* http://hdl.handle.net/21.11116/0000-0003-752A-B. (2019).

47. Virginia Diodes Incorporated. *Waveguide Band Designations* https://vadiodes.com/VDI/pdf/waveguidechart200908.pdf.

48. Butterweck, H. J. & de Ronde, F. C. *Oversized Rectangular Waveguide Components for mm Waves* in *G-MTT International Microwave Symposium Digest* (1967), 35–38. doi:10.1109/GMTT.1967.1122591.

49. Virginia Diodes Incorporated. *WR6.5SGX Datasheet* https://www.vadiodes.com/index.php/en/products/signal-generator?id=678.

50. Senior, T. B. A. Impedance boundary conditions for imperfectly conducting surfaces. *Applied Scientific Research, Section B* **8,** 418. doi:10.1007/BF02920074 (1960).

51. Frei, W. *Using Perfectly Matched Layers and Scattering Boundary Conditions for Wave Electromagnetics Problems* https://www.comsol.com/blogs/using-perfectly-matched-layers-and-scattering-boundary-conditions-for-wave-electromagnetics-problems/.

52. Frei, W. *Ports and Lumped Ports for Wave Electromagnetics Problems* https://www.comsol.com/blogs/ports-and-lumped-ports-for-wave-electromagnetics-problems/.

53. Tischer, F. J. Oversized waveguides and resonators for millimeter waves. *International Journal of Infrared and Millimeter Waves* **9,** 15–27. doi:10.1007/BF01010618 (1988).

54. Ediss, G. A. *Measurements and Simulations of Overmoded Waveguide Components at 70-118 GHz, 220-330 GHz, and 610-720 GHz* in *Fourteenth International Symposium on Space Terahertz Technology* https://ui.adsabs.harvard.edu/abs/2003stt..conf..138E (2003).

55. Eddy Current Technology Incorporated. *Conductivity Of Metals Sorted By Resistivity* http://eddy-current.com/conductivity-of-metals-sorted-by-resistivity/. (1955).

56. Stil, I. *Loss of WR10 Waveguide across 70-116 GHz* in *22nd International Symposium on Space Terahertz Technology* https://pdfs.semanticscholar.org/8d2c/e2f3107dc47eff39806d5bee91fc91a8aa9a.pdf (2012).

57. Lawson, W. G. Theoretical evaluation of nonlinear tapers for a high-power gyrotron. *IEEE Transactions on Microwave Theory and Techniques* **38,** 1617–1622. doi:10.1109/22.60007 (1990).

58. Stutzman, W. & Thiele, G. *Antenna Theory and Design* 299. ISBN: 978-0-471-02590-0 (Wiley, 1998).

59. Teshirogi, T. & Yoneyama, T. *Modern Millimeter-wave Technologies* 87–89. ISBN: 978-1-586-03098-8 (Ohmsha, Limited, 2001).

60. Sage Millimeter Incorporated. *WR-06 Standard Gain Horn Antenna Datasheet* https://www.sagemillimeter.com/content/datasheets/SAZ-2410-06-S1.pdf.

61. Ensinger GmbH. *TECAPEEK ELS nano black* https://www.ensingerplastics.com/de-de/halbzeuge/produkte/peek-tecapeek-els-nano-black.

62. Sage Millimeter Incorporated. *D-Band Waveguide Detector* https://www.sagemillimeter.com/content/datasheets/STD-06SF-PI.pdf.

63. Hesler, J. L. & Crowe, T. W. *NEP and responsivity of THz zero-bias Schottky diode detectors* in *2007 Joint 32nd International Conference on Infrared and Millimeter Waves and the 15th International Conference on Terahertz Electronics* (2007), 844–845. doi:10.1109/ICIMW.2007.4516758.

64. Monorchio, A., Mittra, R. & Manara, G. in *Encyclopedia of RF and Microwave Engineering* (American Cancer Society, 2005). ISBN: 978-0-471-65450-6.

65. Neilson, J. M., Latham, P. E., Caplan, M. & Lawson, W. G. Determination of the resonant frequencies in a complex cavity using the scattering matrix formulation. *IEEE Transactions on Microwave Theory and Techniques* **37,** 1165–1170. doi:10.1109/22.31074 (1989).

A. Transmission through non-uniform waveguides

In Chapter 4 waveguides were introduced in general and in Section 4.4 the mode matching technique [43] was described. Here the more mathematical details are worked out.

A.1. Waveguide step junction

A waveguide step junction (visualised in Figure A.1) is the simplest case of a discontinuity in a waveguide and can be used to model any waveguide with a fixed axis direction. The left side
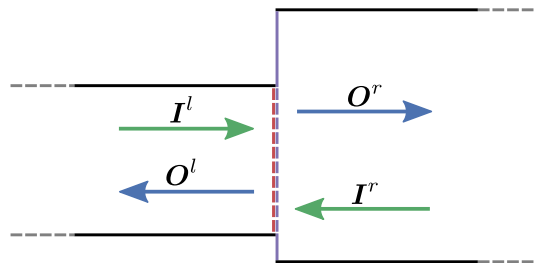

Figure A.1: Cross-section of a waveguide step junction. The red and purple lines indicate the left side cross-section S^l and right side cross-section S^r respectively. $I^{l,r}$ are the vectors of ingoing mode amplitudes and $O^{l,r}$ the vectors of outgoing mode amplitudes.

cross-section S^l is assumed to fit inside the right side cross-section S^r, such that their overlap is again S^l. The transverse fields on both sides of the junction can be written as a sum over the modes given by the particular cross-section and both negative and positive z-direction. Let I be the vector of incoming electric field wave amplitudes on the junction and O the vector of

outgoing amplitudes[1], then

$$E_T^{l,r}(\mathbf{x}) = \sum_n^{N^{l,r}} \left(I_n^{l,r} e^{\mp i k_z z} + O_n^{l,r} e^{\pm i k_z z} \right) \mathbf{e}_n^{l,r}(x,y),$$

$$B_T^{l,r}(\mathbf{x}) = \sum_n^{N^{l,r}} \pm \frac{\mu_0}{Z_n^{l,r}} \left(I_n^{l,r} e^{\mp i k_z z} - O_n^{l,r} e^{\pm i k_z z} \right) \mathbf{h}_n^{l,r}(x,y) \qquad \text{(A.1)}$$

are the transverse fields on the left (l) and right (r) side of the junction. The vectors $\mathbf{e}_n^{l,r}(x,y)$ and $\mathbf{h}_n^{l,r}(x,y) = \mathbf{e}_z \times \mathbf{e}_n^{l,r}(x,y)$ contain the transverse spatial dependence of the specific mode n. In praxis, the number of modes N^l and N^r has to be finite and should be large enough to include all propagating modes. This means that all wave amplitudes of the higher modes are set equal to zero.

Given the incoming mode amplitudes $\mathbf{I}^{l,r}$, a set of $(N_l + N_r)$ equations is needed to connect them to the unknown quantities $\mathbf{O}^{l,r}$. To obtain this set of equations it is useful to first consider the vectors $\mathbf{e}_n^{l,r}(x,y)$ and $\mathbf{h}_n^{l,r}(x,y)$ as basis vectors of a two-dimensional function space of two variables constraint to the cross-section of the waveguide. The scalar products

$$\int_{S^{l,r}} dA \left(\mathbf{f}(x,y) \cdot \left(\mathbf{e}_n^{l,r}(x,y) \right)^* \right) = f_n^{l,r}, \qquad \text{(A.2)}$$

$$\int_{S^{l,r}} dA \left(\mathbf{f}(x,y) \cdot \left(\mathbf{h}_n^{l,r}(x,y) \right)^* \right) = f_n^{l,r}, \qquad \text{(A.3)}$$

where $\int_{S^{l,r}} dA$ is the integral over the cross-section of the waveguide and * means complex conjugation, can be used to compute the components of a given function $\mathbf{f}(x,y)$. The factors in the sum Eq. (A.1) are thus the components of a vector in this space. At the interface of the junction, $z = 0$, the transverse fields need to be continuous

$$E_T^l(\mathbf{x}) = \sum_n^{N^l} \left(I_n^l + O_n^l \right) \mathbf{e}_n^l(x,y) = \sum_n^{N^r} \left(I_n^r + O_n^r \right) \mathbf{e}_n^r(x,y) = E_T^r(\mathbf{x}), \qquad \text{(A.4)}$$

$$B_T^l(\mathbf{x}) = \sum_n^{N^l} \frac{\mu_0}{Z_n^l} \left(I_n^l - O_n^l \right) \mathbf{h}_n^l(x,y) = -\sum_n^{N^r} \frac{\mu_0}{Z_n^r} \left(I_n^r - O_n^r \right) \mathbf{h}_n^r(x,y) = B_T^r(\mathbf{x}). \qquad \text{(A.5)}$$

The scalar products are now used to obtain the $(N^r + N^l)$ equations necessary to determine the outgoing amplitudes. On equation Eq. (A.4) the scalar product with the modes $\mathbf{e}_m^l$ is applied resulting in

$$I_m^l + O_m^l = \sum_n^{N^r} \left(I_n^r + O_n^r \right) \int_{S^l} dA \left(\mathbf{e}_n^r(x,y) \cdot \left(\mathbf{e}_m^l(x,y) \right)^* \right), \qquad \text{(A.6)}$$

where the orthonormality of the $\mathbf{e}_m^l$ was used on the left hand side. The scalar product with the magnetic field mode vectors $\mathbf{h}_m^r$ is applied on equation Eq. (A.5). Again using the orthonor-

---

[1] Eq. (4.7) connects the amplitudes of the magnetic field to the electric field through the wave impedance Z.

mality of $\boldsymbol{h}_m^r$ this produces

$$\frac{1}{Z_m^r}\left(O_m^r - I_m^r\right) = \sum_n^{N^l} \frac{1}{Z_n^l}\left(I_n^l - O_n^l\right)\int_{S^l} dA\left(\boldsymbol{h}_n^l(x,y)\cdot\left(\boldsymbol{h}_m^r(x,y)\right)^*\right),\tag{A.7}$$

where the integration over S^r reduces to an integration over S^l due to $\boldsymbol{h}_m^l$ being zero outside of S^l. The ordinary cartesian scalar product inside the integral simplifies to

$$\boldsymbol{h}_n^l\cdot\left(\boldsymbol{h}_m^r\right)^* = \left(\boldsymbol{e}_z\times\boldsymbol{e}_n^l\right)\cdot\left(\boldsymbol{e}_z\times\boldsymbol{e}_m^r\right)^* = \boldsymbol{e}_n^l\cdot\left(\boldsymbol{e}_m^r\right)^*.\tag{A.8}$$

Equations Eq. (A.6) and Eq. (A.7) can be written in matrix-vector form

$$\begin{aligned}
\boldsymbol{I}^l + \boldsymbol{O}^l &= \mathbb{P}\left(\boldsymbol{I}^r + \boldsymbol{O}^r\right),\\
\boldsymbol{O}^r - \boldsymbol{I}^r &= \text{diag}\left(Z^r\right)\mathbb{P}^\dagger\text{diag}\left(\frac{1}{Z^l}\right)\left(\boldsymbol{I}^l - \boldsymbol{O}^l\right)\\
&\equiv \mathbb{Q}\left(\boldsymbol{I}^l - \boldsymbol{O}^l\right),
\end{aligned}\tag{A.9}$$

where the $(N^l\times N^r)$ matrix

$$(\mathbb{P})_{mn} = \int_{S^l} dA\left(\boldsymbol{e}_n^r(x,y)\cdot\left(\boldsymbol{e}_m^l(x,y)\right)^*\right)\tag{A.10}$$

quantifies the coupling between the modes m and n. The dimensions of the matrix $\mathbb{Q}$ involving the wave impedances are $(N^r\times N^l)$. The above calculation constitutes essentially a change from the basis of modes from one of the waveguide to the basis of modes from the other waveguide.

The scattering matrix (S-matrix)

$$\begin{pmatrix}\boldsymbol{O}^l\\\boldsymbol{O}^r\end{pmatrix} = \mathbb{S}\begin{pmatrix}\boldsymbol{I}^l\\\boldsymbol{I}^r\end{pmatrix} = \begin{pmatrix}\mathbb{S}_{11} & \mathbb{S}_{12}\\\mathbb{S}_{21} & \mathbb{S}_{22}\end{pmatrix}\begin{pmatrix}\boldsymbol{I}^l\\\boldsymbol{I}^r\end{pmatrix}\tag{A.11}$$

connects the outgoing to the incoming waves. Its four block-matrix components are now easily expressed through $\mathbb{P}$ and $\mathbb{Q}$ [64]

$$\begin{aligned}
\mathbb{S}_{11} &= (\mathbb{P}\mathbb{Q} + \mathbb{I})^{-1}(\mathbb{P}\mathbb{Q} - \mathbb{I}),\\
\mathbb{S}_{12} &= 2(\mathbb{P}\mathbb{Q} + \mathbb{I})^{-1}\mathbb{P},\\
\mathbb{S}_{21} &= \mathbb{Q}(\mathbb{I} - \mathbb{S}_{11}),\\
\mathbb{S}_{22} &= \mathbb{I} - \mathbb{Q}\mathbb{S}_{12},
\end{aligned}\tag{A.12}$$

with $\mathbb{I}$ being the identity matrix of the appropriate dimension. A junction of decreasing cross-section can equivalently be treated as one of increasing cross-section by mirroring the junction and switching the indices 1 and 2 after calculating the S-matrix Eq. (A.12). It has been found that the number of modes on both sides of the junction should be in proportion to the radii [44]

$$\frac{N^r}{N^l} = \frac{R^r}{R^l}.\tag{A.13}$$

Then the initial number of modes should be in proportion to the radius of a waveguide in which only the single TE_{11} can propagate.

A.2. Mode coupling parameters

For circular waveguides the solutions to the wave equation (4.4) are given in Eq. (4.9). Using the relation given in Eq. (4.5) and normalising over the cross-section of the circular waveguide gives the following solution for the previously introduced mode vectors $\boldsymbol{e}_{mn}(\rho, \varphi)$ and $\boldsymbol{h}_{mn}(\rho, \varphi)$ of the TE and TM mode, respectively [65]:

$$
\boldsymbol{e}_{mn}(\rho, \varphi) = \frac{\sqrt{2 - \delta_{m0}}}{J_m(\beta_{mn})\sqrt{\pi\left(\beta_{mn}^2 - m^2\right)}} \left[\frac{m}{\rho} J_m\left(\frac{\beta_{mn}\rho}{R}\right)\sin(m\varphi)\boldsymbol{e}_\rho + \frac{\beta_{mn}}{R}J'_m\left(\frac{\beta_{mn}\rho}{R}\right)\cos(m\varphi)\boldsymbol{e}_\varphi \right],
$$

(A.14)

$$
\boldsymbol{h}_{mn}(\rho, \varphi) = \frac{\sqrt{2}}{J_{m-1}(\alpha_{mn})\sqrt{\pi}\alpha_{mn}} \left[\frac{\alpha_{mn}}{R}J'_m\left(\frac{\alpha_{mn}\rho}{R}\right)\sin(m\varphi)\boldsymbol{e}_\rho + \frac{m}{\rho}J_m\left(\frac{\beta_{mn}\rho}{R}\right)\cos(m\varphi)\boldsymbol{e}_\varphi \right],
$$

(A.15)

with the definitions as given in Section 4.2 and δ_{ab} the Kronecker delta.

Using these normalised mode vectors the coupling matrices can be evaluated according to Eq. (A.10). It can be easily verified that there is no mode coupling for different azimuthal wavenumbers because the integral over the angle φ gives a vanishing result. Additionally there is no coupling of TM modes from the smaller side of the junction to TE modes in the larger side. Thus, the mode coupling parameters are written in terms of the radial wavenumber n_1 and n_2, where the index 1 indicates the smaller section [65]:

TE → TE :

$$
P_{n_1 n_2} = \frac{2\frac{R_1}{R_2}\beta_{mn_2}J'_m\left(\beta_{mn_2}\frac{R_1}{R_2}\right)}{J_m(\beta_{mn_2})\sqrt{\left(\beta_{mn_1} - m^2\right)\left(\beta_{mn_2} - m^2\right)}\left(1 - \left(\frac{\beta_{mn_2}}{\beta_{mn_1}}\frac{R_1}{R_2}\right)^2\right)},
$$

(A.16)

TE → TM :

$$
P_{n_1 n_2} = -\frac{2mJ_m\left(\alpha_{mn_2}\frac{R_1}{R_2}\right)}{\alpha_{mn_2}J_{m+1}(\alpha_{mn_2})\sqrt{\beta_{mn_1}^2 - m^2}},
$$

(A.17)

TM → TM :

$$
P_{n_1 n_2} = -\frac{2J_m\left(\alpha_{mn_2}\frac{R_1}{R_2}\right)}{\alpha_{mn_2}J_{m+1}(\alpha_{mn_2})\left(1 - \left(\frac{\alpha_{mn_1}}{\alpha_{mn_2}}\frac{R_2}{R_1}\right)^2\right)}.
$$

(A.18)

B. Additional estimates for the waveguide optimisation

In Chapter 5 the oversized waveguide components were optimised and a total loss was calculated. A few additional sources of loss already included in the summary of Section 5.6 are considered in more detail here.

B.1. Hole in the creation trap

In order to have a direct path from the glass sphere containing the ^{3}He to the Penning traps a hole in one of the electrodes with $r = 3$ mm is needed. As this hole introduces an asymmetry into the waveguide, see Figure 5.11, a cylindrical symmetric FEM calculation is not directly possible. Nevertheless, by modelling the hole as a complete gap of waveguide with a length of its diameter it is still possible to make an estimate of the loss the hole introduces. Figure B.1 shows the loss calculated with COMSOL. The loss introduced does not show any large resonances and is bounded by about -2.5 dB.

B.2. Horizontal displacement of microwave horns

It can not be assured that the standard gain horn connected to the WR6 waveguides is perfectly aligned horizontally with respect to the 4 mm oversized waveguide inside the setup, compare Figure 5.7. As any horizontal displacement destroys the cylindrical symmetry this can not be calculated with a cylindrically symmetric FEM geometry. A full three dimensional calculation is to expensive in terms of computation time, leaving a simplified two dimensional geometry as an alternative. For this a 8 mm wide waveguide without a horn is placed 3 cm away from a standard gain horn with 9 mm opening radius and 3.8 cm length. The standard gain horn is connected to a 800 μm waveguide.

Figure B.2 shows the results of the FEM calculation for varying displacements. Here the transmission was averaged over the frequency range from 148 to 166 GHz. There is not much additional loss from the displacement of the waveguide relative to the horn. Apparently, as the horn is transmitting the microwaves into a solid angle which is larger than the angle cov-

ered by the 8 mm wide waveguide, a horizontal displacement does not reduce the amount of microwaves picked up by much.
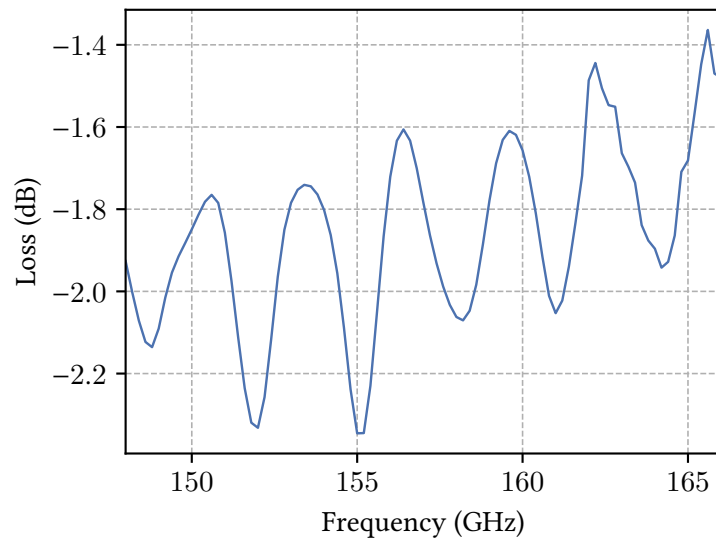

Figure B.1: Loss calculated with COMSOL for a waveguide with a radius of 3 mm and a 8 mm gap.
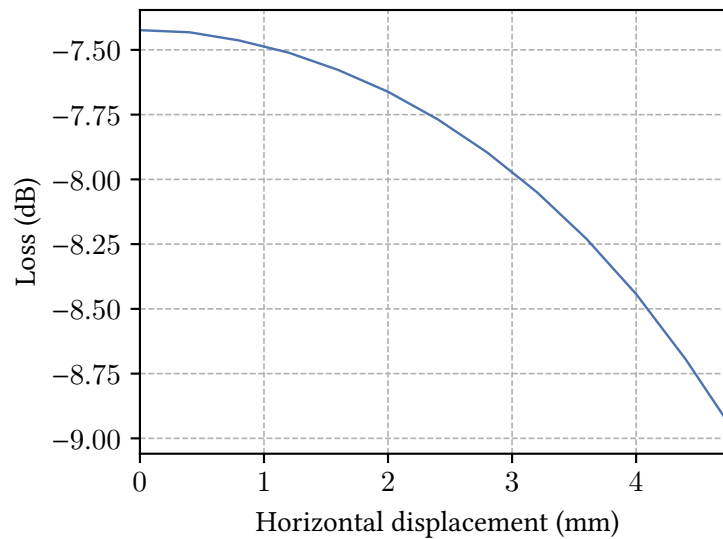

Figure B.2: Loss of the fundamental mode through the geometry described in the text for varying horizontal displacements.

Danksagung

Ich möchte mich hier bei allen bedanken, die mich während meiner Zeit als Masterstudent am MPIK unterstützt haben.

Zu aller erst möchte ich mich bei Klaus Blaum für die tolle Betreuung der Masterarbeit bedanken! Die Arbeit in der Abteilung hat mir sehr viel Spaß gemacht und ich bin sehr froh auch als Doktorand weiter in dieser tollen Abteilung bleiben zu können.

Vielen Dank auch an Wolfgang Quint für die sehr unkomplizierte Bereitschaft das Zweitgutachten meiner Arbeit zu erstellen.

Einen großen Dank gebührt natürlich allen Mitgliedern des 3-Helium Experiments. Danke Andi für die große Unterstützung von Anfang an und das Korrekturlesen der Masterarbeit. Als Gruppenleiter des 3-Helium Experiments warst du immer eine große Hilfe und selbst wenn ich ein paar wirre Gedankengänge nicht ordentlich in Worte fassen konnte, hast du dir doch die Zeit genommen mir zuzuhören. Danke Antonia, für die gute Zusammenarbeit und deine bewundernswerte Geduld beim Ionen laden. Danke Marius, für die große Hilfe bei vielen technischen Sachen, da hast du mir noch einiges Vorraus! Ich freue mich auf die nächsten Jahre bei denen ich als Doktorand mit euch zusammenarbeiten werde. Vielen Dank auch an die ehemaligen Mitglieder Tom und Alex für die freundschaftliche Unterstützung.

Weiterhin möchte ich mich bei den Mitgliedern von PENTATRAP, Rima, Kathrin, Daniel, Menno und Christoph sowie nochmals Marius für die unterhaltsamen Gespräche beim Essen, und für die Aktivitäten abseits der Arbeit bedanken. Ist echt super, dass wir so eine tolle Gruppe haben.

Zuletzt möchte ich mich bei meinen Eltern und meinen Mitbewohnern in Heidelberg für die große Unterstützung während der langen Zeit des Physikstudiums bedanken. Ohne euch hätte ich das nicht geschafft.